

1
2 **The Cauchy 5 Small, Low-Volume Lunar Shield Volcano: Evidence for Volatile**
3 **Exsolution-Eruption Patterns and Type 1/Type 2 Hybrid Irregular Mare Patch**
4 **(IMP) Formation**

5 **Le Qiao^{1,2}, James W. Head², Lionel Wilson³, Zongcheng Ling¹**

6 ¹Shandong Key Laboratory of Optical Astronomy and Solar-Terrestrial Environment, School of
7 Space Science and Physics, Institute of Space Sciences, Shandong University, Weihai,
8 Shandong, 264209, China.

9 ²Department of Earth, Environmental and Planetary Sciences, Brown University, Providence, RI
10 02912, USA.

11 ³Lancaster Environment Centre, Lancaster University, Lancaster LA1 4YQ, UK.

12 Corresponding authors: Le Qiao (leqiao.geo@gmail.com), Zongcheng Ling (zcling@sdu.edu.cn)

13 **Key Points:**

- 14 • Cauchy 5 small shield volcano displays two types of IMPs: Type 1 (mound + floor) in its
15 summit pit and Type 2 (pit only) on its flanks
- 16 • Small edifice volume maximizes volatile exsolution and favors strombolian lava lake
17 activity and emplacement of vesicular flank lavas
- 18 • Relationships at Cauchy 5 summit and flanks provide a link to understanding the genetic
19 relationship between the two IMP sub-types
20

21 **Abstract**

22 The lunar shield volcano Cauchy 5, sitting at the low diameter-height-volume end of the
23 population, is the only known example containing two different types of Irregular Mare Patches
24 (IMPs) in very close association: 1) the pit crater interior Type 1 IMP composed of bleb-like
25 mounds surrounded by a hummocky and blocky floor unit, and 2) Type 2 IMPs, small, often
26 optically immature pits <~5 meters deep, located on the generally block-deficient shield flanks.
27 A four-phase lunar magma ascent/eruption model predicts that during a relatively brief eruption,
28 low magma rise rates maximize volatile exsolution in lava filling the pit crater. Bubble-rich
29 magmas overtop the pit crater and form extremely bubble-rich/vesicular flows on the shield
30 flanks. Exposure of the flanking flows to vacuum produces a fragmental layer of exploded glassy
31 bubble walls. Subsequent second boiling upon cooling of the flanking flow interiors releases
32 additional volatiles which migrate and collect, forming magmatic foams and gas pockets. As
33 magma rise rates slow, trapped gas and magmatic foam build up below the cooling pit crater
34 floor. Magmatic foams are extruded to form Type 1 IMP deposits. Type 2 IMPs on the flanks are
35 interpreted to be due primarily to subsequent impacts causing collapse of the flow surface layer
36 into the extremely vesicle- and void-rich flow interior. Anomalously young pit crater floor/shield
37 flank crater retention ages compared with surrounding maria ages may be due to effects of
38 Cauchy 5 substrate characteristics (extreme micro- and macro-porosity, foamy nature and glassy
39 auto-regolith) on superposed crater formation and retention.

40 **Plain Language Summary**

41 A group of distinctive and unusual features in the lunar maria known as “Irregular Mare Patches”
42 (IMPs) are of two types: Type 1 (“mound + floor”) usually occurring in volcanic pit craters and
43 related depressions, and dated to less than 100 Ma old, and Type 2 (“pit only”) occurring as
44 scattered pits in localized areas of the lunar maria and too small to obtain ages. We investigated
45 Cauchy 5, a small lava shield that is anomalous in that both Type 1 and Type 2 IMPs occur in
46 very close association. Models of magma ascent and eruption in small-volume, low-volume-flux
47 mare basalt eruptions show that gas exsolution is optimized. Gas release patterns and pit crater
48 lava lake behavior produce Type 1 IMPs on the lava lake floor and Type 2 IMPs on the shield
49 volcano flanks from void collapse and subsequent impacts. The extremely vesicular, void-rich
50 and foam-like nature of the lava lake floor and shield flank flows forms a substrate whose
51 characteristics are predicted to significantly influence the formation and degradation of
52 superposed impact craters. This potentially causes the IMPs to appear to be much younger than
53 the adjacent mare units.

54 **1. Introduction and Background:**

55 **1.1. Lunar Mare Volcanism: Styles of Emplacement and Duration of Process in Lunar** 56 **History**

57 Lunar mare basalt volcanism represents a major phase of secondary crust formation (Taylor,
58 1989) in the evolution of the Moon (Wieczorek et al., 2006). Eruptions vary in their associated
59 surface morphology (pit craters, cones, small shields, long lava flows, pyroclastic blankets) and
60 inferred eruption conditions (intrusive, effusive, explosive) (Figure 1). Models of the generation,
61 ascent and eruption of lunar basaltic magmas (e.g., Wilson & Head, 1981; Head & Wilson, 1992,
62 2017; Wilson & Head, 2017a,b; Rutherford et al., 2017; Wilson et al., 2019) have provided a
63 predictive basis to relate dike emplacement events to near-surface and surface mare basalt

64 morphologic features and structures (Head & Wilson, 2017). In addition, detailed models of the
 65 stages or phases in individual mare basalt eruptions (Wilson & Head, 2018) can be used to place
 66 individual eruptive morphologic features into both dike emplacement scenarios (Figure 1) and
 67 the sequence and dominant phases characterizing the eruption.

68 Critically important to understanding the thermal evolution of the Moon is the time of onset,
 69 peak flux and cessation of the eruptive activity associated with lunar mare volcanism. The vast
 70 majority of basaltic volcanism occurred between 3.9 and 3.1 Ga ago and cessation is generally
 71 thought to have occurred more than a billion years ago (Hiesinger et al., 2011) (see Figure 1 in
 72 Head & Wilson, 2017). Recently, the discovery and documentation of dozens of morphologically
 73 fresh, optically immature features associated with the lunar maria, termed Irregular Mare Patches
 74 (IMPs) (Braden et al., 2014), has challenged this conventional view. Superposed impact crater
 75 size-frequency distribution (CSFD) data for the three largest IMPs yield ages of 18, 33 and 58
 76 Ma (Braden et al., 2014), all within the last two percent of lunar history and raising the question:
 77 Could the Moon be volcanically active today?

78 **1.2. Irregular Mare Patches (IMPs) and Implications for the Duration of Mare Volcanism** 79 **in Lunar History**

80 *1) Background and initial interpretation:* The most prominent of the lunar IMPs, the
 81 enigmatic Ina structure (18.65°N, 5.30°E), is composed of a distinctive series of bleb-like
 82 mounds and intervening optically immature (low levels of space weathering spectral effects on
 83 soil maturation) hummocky and blocky floor units, and has intrigued lunar scientists for decades
 84 following its discovery on Apollo photographs in the 1970s (Whitaker, 1972). Investigations
 85 using high-resolution Lunar Reconnaissance Orbiter Narrow Angle Camera (LROC NAC)
 86 images identified dozens of lunar IMPs, all with textures and structures resembling Ina (Stooke,
 87 2012; Braden et al., 2014; Zhang et al., 2018). Qiao et al. (2019b) recently gathered IMP
 88 identifications from multiple prior studies and presented an updated catalog of more than eighty
 89 IMPs. Collectively, these features range from 100 m to 5 km in maximum dimension and all
 90 occur in association with the lunar maria. To improve our understanding of the entire IMP
 91 population, Qiao et al. (2019b) surveyed the detailed geological characteristics and structures of
 92 each cataloged IMP feature and derived a preliminary classification scheme for IMP
 93 characteristics. In this scheme, all the mapped IMPs can be subdivided into two categories. Type
 94 1 IMPs are a small number ($n = 5$) of larger features (2–5 km in dimension) composed of a
 95 combination of positive-relief mounds emplaced on surfaces consisting of rough hummocky
 96 terrains (“mound + floor” type or mound-type). Type 1 IMPs are usually related to small shield
 97 volcano summit pit craters and vent-like structures (e.g., Ina and Sosigenes). Type 2 IMPs
 98 comprise a much larger number ($n = 76$) of smaller features (60 m to 1.2 km in length, average
 99 greatest dimensions less than 300 m) and are composed of rough, bright pitted terrains (“pit
 100 only” type or pit-type), typically having no clear relation to a small shield summit pit crater or
 101 vent (true of at least 67 IMPs among the updated catalog of 81 IMPs by Qiao et al., 2019b).

102 The five large Type 1 IMPs, Ina, Sosigenes, Cauchy 5, Nubium and Maskelyne (2–5 km in
 103 maximum dimension), all have isolated smooth mounded units surrounded by rough floor
 104 terrains (e.g., Schultz et al., 2006; Garry et al., 2012; Braden et al., 2014; Stopar et al., 2017;
 105 Qiao et al., 2019b) and are of sufficient size to obtain CSFD-based model ages. Braden et al.
 106 (2014) found that the smooth mound deposits associated with three of these IMP features gave
 107 model ages all younger than 100 Ma (Sosigenes, 18 ± 1 Ma; Ina, 33 ± 2 Ma; Cauchy 5, 58 ± 4

108 Ma). Valantinas et al. (2018) recently reported a model age of 48 ± 5 Ma for the Nubium IMP
109 mound terrains. On the basis of these ages and other observations, including optical freshness
110 and distinctive mound-like shapes with sharp boundaries, Braden et al. (2014) interpreted the
111 unusual morphology of these features to represent small mare volcanic eruptions that occurred
112 “significantly after the established cessation of lunar mare basaltic volcanism”. Such
113 geologically very recent eruptions would suggest a prolonged duration of lunar volcanism that
114 appears to be in conflict with the established thermal evolution of the Moon (e.g., Wieczorek et
115 al., 2006). Braden et al. (2014) envisioned a process in which the relatively steep-sided mounds
116 represent small basalt extrusions with the stratigraphically lower “uneven” deposits as
117 fragmented basalt or lava lake crust within the eruptive vent formed during the collapse of the
118 vent.

119 The vast majority of IMPs are much smaller than the five largest (in maximum dimension)
120 mentioned above and cannot be dated with the CSFD techniques (the remaining population
121 averaged <300 m in longest dimension; average length = 275 m, $n = 76$; Qiao et al., 2019b).
122 These small Type 2 IMPs share some of their morphologic characteristics with the large Type 1
123 IMPs, while also showing many morphological and geologic context differences. The smaller
124 Type 2 IMPs are characterized by many irregularly shaped, rough textured pits and lack the
125 characteristic bleb-like raised mound structures seen at the five largest Type 1 IMPs. The
126 smaller Type 2 IMPs are also generally not related to volcanic pit craters or vents. The larger
127 Type 1 IMPs, however, are commonly associated with volcanic pit craters and often have
128 isolated smooth raised mounds surrounded by rough floor terrains; these smooth mounded
129 deposits always have lobate margins and steep boundary slopes, and are interpreted (Braden et
130 al., 2014) to be superposed on the surrounding uneven floor deposits. So, it is unknown whether
131 the two IMP sub-types have similar or different origins due to the fact that 1) the morphologies
132 of the sub-types have some similarities, but are also different in many aspects (the Type 2 IMPs
133 typically do not have individual mounds surrounded by rough terrain), 2) the Type 1 and 2 IMPs
134 do not occur in close proximity, and 3) the Type 2 IMPs are generally too small to date
135 confidently and thus cannot be assumed to be of the same young age or origin (Braden et al.,
136 2014).

137 2) *Subsequent and additional interpretations for the origin of IMPs*: Following the
138 identification and documentation of over eighty IMPs and the dating of the several large Type 1
139 IMPs, interpretations different from that of Braden et al. (2014) have also been proposed. These
140 include pyroclastic deposition (Carter et al., 2013), contemporaneous emplacement with the
141 adjacent ancient mare deposits, with deposits of elevated blockiness (Bennett et al., 2015), some
142 style of explosive process (either pyroclastic deposition or removal of surface materials by out-
143 gassing) (Schultz et al., 2006; Elder et al., 2017) and some geological process other than
144 Copernican-age lava flow emplacement (Neish et al., 2017). However, these subsequently and
145 previously proposed IMP origin models are either very general (e.g., Bennett et al., 2015; Elder
146 et al., 2017; Neish et al., 2017), or have not been able to reproduce all the observed IMP
147 characteristics (e.g., Schultz et al., 2006; Garry et al., 2012; Braden et al., 2014; see a more
148 detailed assessment in Qiao et al., 2018).

149 Wilson and Head (2017a) pointed out that lunar volcanic eruptions occur in conditions very
150 different from those on Earth, especially in the consideration of lower lunar gravity and lack of
151 an atmosphere (Head & Wilson, 2017; Wilson & Head, 2017b), which results in unusual
152 volcanic deposits neither predicted by models nor observed on Earth in the final phases of

153 eruptions. Wilson and Head (2017a) assessed the physical volcanology of the final stages of
154 eruptions in small shield volcano summit vent floors, such as Ina, and showed that many
155 observed characteristics of Type 1 IMPs could be explained by these final-stage eruptive
156 activities. Specifically, as the magma ascent rate approaches zero, volatiles exsolve in the top
157 part of the dike and lava lake to form a highly vesicular foam. As the dike begins to close due to
158 the elastic response of the crust, the foam is squeezed upward and extruded through cracks in the
159 chilled and porous lava lake crust as the crust is deformed. Wilson and Head (2017a) interpreted
160 the hummocky and blocky floor units at lunar Type 1 IMPs as the very porous solidified lava
161 lake crust, and the final-stage magmatic foam extrusions as the mechanism that produces convex
162 mounds; aerogel-like foam physical properties modify typical impact cratering and regolith
163 production on the mounds, potentially retaining a youthful surface (see the mechanisms in more
164 details in Wilson & Head, 2017a; Qiao et al., 2017, 2018, 2019a).

165 Qiao et al. (2017, 2019a) analyzed the Ina feature (a Type 1 IMP) and confirmed that the
166 structure was the summit pit crater of a ~22 km diameter, ~3.5 Ga old shield volcano (Strain &
167 El-Baz, 1980). The morphology of the mounds and rough floor of Ina were interpreted to be
168 consistent with the lava lake and magmatic foam formation scenario (Wilson & Head, 2017a).
169 Furthermore, when the effects of impacts into magmatic foam were taken into consideration
170 (crushing of the foam, minimal ejecta and much smaller diameter crater), the CSFD of the
171 mounds was more consistent with that of the ancient ~3.5 Ga old shield volcano on which Ina pit
172 crater resides. Qiao et al. (2017, 2019a) concluded that Ina represented an example of the
173 unusual eruption styles likely in summit pit craters during late-stage extrusion of magma made
174 foamy by the unusual low-gravity, essentially zero-atmospheric pressure lunar environment
175 (Wilson & Head, 2017b). Qiao et al. (2018) also analyzed the second of the large Type 1 IMP
176 features, the elongate Sosigenes depression, a structure associated with a dike emplacement
177 event in Mare Tranquillitatis, and reached similar conclusions. Thus, the proposed late-stage
178 degassing and magmatic foam formation mechanism (Wilson & Head, 2017a; Qiao et al., 2017,
179 2018, 2019a) offers an alternative interpretation to account for the main features of the two major
180 occurrences of Type 1 IMPs, without resorting to lunar volcanic activity occurring in the last 100
181 million years.

182 **1.3. The Cauchy 5 Small Shield Volcano: A Hybrid Example of the Two Types of Lunar** 183 **IMPs**

184 Small lunar shield volcanoes (Head & Gifford, 1980) represent the low-volume, low-
185 effusion rate end of the lunar mare basalt eruption spectrum (Head & Wilson, 2017; their section
186 3.5.2) (Figure 1). In the current analysis, we chose to investigate the Cauchy 5 small shield
187 volcano in Mare Tranquillitatis because: 1) it has both a large Type 1 IMP in its summit pit crater
188 (Braden et al., 2014) and a population of over a hundred small Type 2 IMPs on the shield flanks,
189 2) it has an elongate summit pit crater whose depth reaches several tens of meters below the
190 shield into the pre-shield substrate, and 3) superposed impact craters yield a CSFD interpreted to
191 represent an age of ~58 Ma (Braden et al., 2014), more than three billion years younger than
192 surrounding mare basalt units (Hiesinger et al., 2011). Analysis of Cauchy 5 offers the
193 opportunity to assess: 1) the origin of IMPs, 2) the ages of IMPs and 3) the relationships between
194 the two sub-types of IMPs in terms of their mode(s) of origin through physical volcanology
195 analyses and geological characterization.

196 We first describe the setting and characteristics of the Cauchy 5 small shield volcano and its
197 related deposits and features. Secondly, we explore the predictions of models for the intrusion
198 and eruption of dikes producing small-volume eruptions (Head & Wilson, 2017) and the nature
199 of the predicted effusion and volatile release phases in such eruptions (Rutherford et al., 2017;
200 Wilson & Head, 2018). We then compare these predictions with the characteristics of the Cauchy
201 5 small shield volcano and the two types of IMP, and conclude with a discussion of the
202 formation of Cauchy 5 and the origin of the unusual ages of its IMP populations.

203 **2. The Cauchy 5 Small Shield Volcano and Associated Type 1 and Type 2 IMPs: Geologic** 204 **Setting and Characteristics**

205 The Cauchy 5 small shield volcano, located in Mare Tranquillitatis (7.169°N, 37.592°E)
206 (Figures 2 and 3), is a circular mound about 5–6 km in base diameter and ~40 m high at its
207 summit (Figure 4). The flanks of the small shield slope away from the summit pit crater to the
208 base of the shield (2–6° slopes, 15 m baseline), where they join the regional generally flat mare
209 (black arrows in Figure 4b). The surrounding mare surface slopes slightly down to the east
210 (Figures 3a and 4b). The Cauchy 5 small shield has a total volume of ~0.5 km³. Cauchy 5 is
211 generally typical of the population of small shield volcanoes on the Moon (Figure S1; Head &
212 Gifford, 1980; Tye & Head, 2013; Wöhler et al., 2006, 2007; Lena et al., 2007, 2008; Liu et al.,
213 2018), but lies at the lower end of the diameter, height and volume ranges typical of these
214 features (Figure S1).

215 Cauchy 5 displays an elongate summit pit crater (Figures 3, 4a, 5 and 6), ~0.75 × 2.5 km
216 wide and ~75 m deep, oriented in a WNW direction (Figure 5). The pit crater floor is about 65–
217 75 m below the rim of the pit crater and about 45–60 m below the elevation of the surrounding
218 maria. This configuration is different from that of the much larger ~22 km wide Ina small shield
219 volcano (compare Figures 4a, b and 4c, d). At Ina, the shield summit stands more than 300 m
220 above the surrounding mare surface and the summit pit crater floor is ~20–50 m below the pit
221 crater rim, more than 250 m above the surrounding mare on which the shield is constructed
222 (Figures 4c and 4d; Qiao et al., 2017, 2019a).

223 One of the three major Type 1 “mound + floor” IMPs identified by Braden et al. (2014)
224 occupies the summit pit crater of Cauchy 5 shield volcano (Figures 3 and 5; #3 IMP in Braden et
225 al.’s Table S1). In a manner similar to the two other largest Type 1 IMPs, Ina (#2) and Sosigenes
226 (#1), the Cauchy 5 summit pit crater contains a combination of extensive mound-like deposits on
227 the pit crater floor, and rough textured and optically immature floor and adjacent wall material
228 (Figure 5). In addition to its similarities to Ina and Sosigenes, Cauchy 5 also shows some
229 differences. First, both Ina and Sosigenes show a generally distinctive difference between the
230 mare plains surrounding the pit crater/graben, and the mound and bright/rough terrain that
231 characterize the pit crater floor (Garry et al., 2012; Braden et al., 2014; Qiao et al., 2017, 2018,
232 2019a). In the case of Cauchy 5, the generally elongate, tongue-depressor shape of the vent is
233 perturbed to the west and north by an extension of the pit crater, although at a level ~30–45 m
234 shallower than the deepest part of the pit in the southeast (Figures 5 and 6). This configuration
235 suggests that there may have been at least two topographic levels for lava partially filling the
236 lava lake; a deeper one to the southeast (approximately between contours -895 m and -910 m in
237 Figure 5d) and a much shallower one to the northwest (approximately between contours -880 m
238 and -865 m in Figure 5d). In addition, an ~750 × 850 m, 30–35 m deep topographic
239 extension/opening occurs in the northern part of the pit crater (Figure 5), characterized by

240 comparable or slightly lower elevations (down to contour -880 m in Figure 5d) than for the
241 northwest part of the vent floor (Figures 3, 5 and 6). This feature may have been an exit breach
242 for flows leaving the summit pit crater lava lake, as seen in some terrestrial small shield
243 volcanoes (e.g., Tilling, 1987).

244 Secondly, mound and rough terrain textures typical of the interior of the Ina and Sosigenes
245 depressions also occur in Cauchy 5 on an $\sim 750 \times 800$ m area on the NW rim (Figure 7), and in a
246 $\sim 1.3 \times 1.4$ km area to the north, within the rim depression and to its west and north (Figure 5).
247 These distinctive morphologic occurrences and the different topographic levels that characterize
248 the pit crater floor, are also similar to evidence for multiple levels in erupting, fluctuating and
249 receding terrestrial lava lakes in small shield volcanoes and vent areas (e.g., Peck et al., 1979;
250 Tilling, 1987; Wolfe et al., 1987; Tilling et al., 1987, their Figure 16.8).

251 Thirdly, unlike Ina and Sosigenes, smaller, pit-like Type 2 IMPs (rough and pitted terrains
252 in small patches) occur in two broad regions on the summit rim and flanks of the Cauchy 5 small
253 shield volcano (Figure 8): 1) an $\sim 1 \times 4$ km broad belt on the northern shield flank, located at a
254 distance from the topographic breach in the elongate pit crater (pink polygons in Figure 8a and
255 local map in Figure 8c), and 2) a concentric zone adjacent to the southeastern edge of the
256 elongate pit crater and extending up to 0.5 to 2 km from the pit crater rim (blue polygons in
257 Figure 8a and local map in Figure 8d). Examination of the southeastern rim pit-type IMP region
258 (Figure 8d) shows that it is characterized by over 70 small irregular IMP-like pits, while the
259 northern Cauchy 5 shield flank pit-type IMP region (Figure 8c) is also populated by ~ 70 small
260 irregular pits. Many of these small pits occur on the interior steep walls of depressions,
261 immediately adjacent to the depression rim crest (Figure 8d). The two small-pit-type IMP
262 occurrences show similar length-frequency distribution patterns (Figure 8b) (112 m mean and 96
263 m median lengths for the north flank small pits; 118 m mean and 94 m median lengths for the
264 southeastern rim small pits) and areal density ($\sim 14\text{--}18$ pits per km^2). We focused on all relatively
265 large Type 2 IMP pits (>50 m in length) on relatively flat surfaces (a total of 65 pits; these do not
266 include pits on the upper walls of depressions) and measured their pit depth from LROC NAC
267 DTM topography by deriving the elevation difference between the average elevation of the
268 surrounding surface (5–15 m exterior buffer area from the pit edge) and the minimum elevation
269 of the pit interior. The measured pit depths (Figure 8e) range from ~ 1 to ~ 6 m, with a mean pit
270 depth of ~ 3 m. Virtually all pits (95%) have depths of <5 m. More importantly, the pit-type IMP
271 features seen in these two localities are very similar in morphology to those Type 2 IMPs
272 documented in the updated Braden et al. (2014) IMP catalog (Qiao et al., 2019b) (compare the
273 Cauchy 5 rim and flank small pit-type IMPs to occurrences #8, 10-19, 22-25, 27-32, 34, 35, 37,
274 39-40, 41-49, 51-56, 59-61, 63 and 65-70 small IMP examples in the Braden et al. (2014) list
275 (their Table S1)). However, these small pits at Cauchy 5 are generally smaller than the Type 2
276 IMPs cataloged by Qiao et al. (2019b), which have a mean and median length of 275 m and 200
277 m, respectively.

278 Remote sensing data provide further characterization of the Cauchy 5 small shield. Ground-
279 based Arecibo radar observations (Campbell et al., 2010) show that the Cauchy 5 shield flank is
280 characterized by fine-grained, block-poor materials (Carter et al., 2013; Figure S4), in contrast to
281 the basalt bedrock-derived regolith substrate typical of surrounding regional mare deposits.
282 Carter et al. (2013) interpreted these characteristics as possibly indicating the presence of
283 pyroclastic deposits on the flanks of the Cauchy 5 shield volcano. LRO Diviner thermophysical
284 mapping also shows that the surface between the Type 2 IMPs on the Cauchy 5 shield flank is

285 less blocky than the highly pitted surfaces at the northern base edge of the shield (Elder et al.,
286 2017). The Cauchy 5 small shield and the surrounding mare plains are similar in surface
287 mineralogy (high-titanium basalts; Staid & Pieters, 2000), suggesting a mare basalt composition
288 comparable to that of other areas of Mare Tranquillitatis.

289 Mapping of reflectance at 750 nm and optical maturity based on Kaguya Multiband Imager
290 (MI) spectrometer data (20 m/pixel; Ohtake et al., 2008) and the algorithm of Lemelin et al.
291 (2015) was undertaken for the relatively extensive pits (dominantly on the interior steep walls of
292 many depressions) at the southeastern rim of Cauchy 5 (Figure 9). These data show that these
293 mapped small IMP-like pits are generally more reflective and optically immature than the inter-
294 pit terrains and surrounding mare, similar to observations of the hummocky and blocky floor
295 units at the interior of several large Type 1 IMPs such as Ina and Sosigenes (Strain & El-Baz,
296 1980; Schultz et al., 2006; Staid et al. 2011; Garry et al., 2013; Bennett et al. 2015; Qiao et al.,
297 2018, 2019a). In addition, these optical property maps reveal obvious reflectance and optical
298 maturity variations among these mapped pits (noted by arrows in Figure 9).

299 The flat mare unit surrounding Cauchy 5 is dated to over three billion years in age
300 (Hiesinger et al., 2011), comparable with our CSFD dating result for a 5×5 km² mare area north
301 of Cauchy 5 (Figure S2). We performed crater-counting analyses (craters ≥ 10 m in diameter) on
302 the inter-pit surface at the north edge of the Cauchy 5 small shield, where abundant small pits are
303 observed, using LROC NAC images (Figures 10a and c). The resulting crater populations are
304 presented in the standard cumulative (Figure 10b) and relative (Figure S3) size-frequency
305 distribution plots (the conventional methodology utilized in the community, e.g., Crater Analysis
306 Techniques Working Group, 1979; Fassett, 2016). For comparison, we also transferred the map
307 of the crater count working area on the northern shield flank onto the adjacent mare surface and
308 counted the superposed impact craters there (Figures 10a, b and d). The shield flank area shows a
309 much lower crater density for craters ≥ 10 m in diameter when compared with the surrounding
310 basaltic mare surface, especially at larger diameter ranges. Lunar chronology function (CF) and
311 production function (PF) (Neukum et al., 2001) fitting of these shield flank craters yields a
312 model age of hundreds of million years (160 Ma), significantly younger than the surrounding >3
313 Ga old ancient mare reported previously (Hiesinger et al., 2011). The CSFD plot of flank craters
314 (black crosses in Figure 10b) does not follow the isochron curve exactly, which is probably
315 related to the fact that a lot of craters are destroyed/obscured by collapse upon impact. (Note that
316 we do not calculate a model age from craters in the surrounding mare count area closely adjacent
317 to the small shield (red polygon in Figure 10a) as this dating analysis suffers from both the
318 problems associated with the small crater counting area and the very small number of impact
319 craters used to derive the age estimate.) In summary, three different CSFD ages are derived for
320 the Cauchy 5 small shield area: 1) ~ 54 Ma for the Cauchy 5 pit crater interior (Braden et al,
321 2014), 2) ~ 160 Ma for the Cauchy 5 shield flank and 3) at least 3000 Ma for the mare areas
322 adjacent to Cauchy 5 (here and in Hiesinger et al., 2011).

323 Utilizing this information on the setting, characteristics and apparent ages of Cauchy 5 and
324 its surroundings, we now turn to models of the generation, ascent and eruption of magma in a
325 small shield volcano environment in order to assess predictions that might be helpful in the
326 interpretation of Cauchy 5's observed deposits and structures (Figures 2-7), and the population of
327 Type 1 and Type 2 IMPs (Figures 8-10).

328 **3. Models of Generation, Ascent and Eruption of Magma for Lunar Small Shield Volcanoes**

329 Lunar small shield volcanoes are generally interpreted to be constructed from relatively low-
330 effusion-rate, cooling-limited lava flows erupting from a centralized vent and still-active and
331 evolving summit pit crater (e.g., Head & Gifford, 1980; Wilson & Head, 2017b; Head & Wilson,
332 2017). In the context of dikes intruding from the mantle into the shallow crust and erupting onto
333 the surface (Figure 1), small shields are interpreted to lie in the range between small-volume
334 dikes that penetrate to the near-surface and stall, producing pit craters, graben and perhaps small
335 cones (Figures 1a-c), and large-volume dikes that penetrate to the surface to produce large-
336 volume, high-effusion rate eruptions (Figure 1f). Within this category, volumes and effusion
337 rates can range from very low (smaller shields) to low (larger shields) (compare Figures 1d and
338 1e).

339 The characteristics of the four eruption phases during a *typical lunar mare basalt eruption*
340 (Wilson & Head, 2018) (Figure 11A) are as follows: In Phase 1, the dike penetrates to the
341 surface and very rapidly explosively vents the gas and foam that have accumulated at the top of
342 the dike during its ascent. In Phase 2, the dike base continues to rise, forcing very large quantities
343 of magma out of the vent at very high effusion rates, creating a very vigorous hawaiian fire
344 fountain eruptive phase. During Phase 3, the dike equilibrates, accompanied by a decrease in
345 magma rise speed and flux, and undergoes a transition from hawaiian to strombolian activity
346 (Parfitt & Wilson, 1995). The vast majority of the magma extruded to the surface during the
347 eruption is emplaced during Phases 2 and 3. The volatile content of the erupted distal lava flows
348 during Phase 3 and most of Phase 4 is very low due to their having lost volatiles during the
349 hawaiian fire-fountain stage of Phase 3. During Phase 4, magma rise speed decreases to <1 m/s
350 and the volume flux of the extruded magma decreases substantially. Due to the very much lower
351 rise rate in Phase 4, explosive activity is confined to the strombolian bursting of large bubbles of
352 CO₂ formed by coalescence, during the slow magma ascent, of small bubbles released at great
353 depth in the dike; shallow-nucleating volatiles (water and sulfur compounds, Rutherford et al.,
354 2017) remain as bubbles in the magma arriving at the top of the dike, causing the extruded lava
355 to be highly vesicular.

356 These four eruption phases are predicted to vary in importance and magnitude during the
357 *low-volume, low-effusion rate eruptions typical of small shield formation*, particularly for the
358 lower end of the volume range indicated for the small (5-6 km diameter), low elevation (~40
359 meters), low volume (~0.5 km³) Cauchy 5 shield. A comparison of the four eruption phases in
360 such a low-volume, low-effusion rate small shield eruption and the more typical larger-scale
361 mare basalt eruption is shown in Figures 11. Low-volume, low-effusion rate eruptions are
362 dominated by Phases 1 and 4 due to the very small total volume of erupted magma and the
363 correspondingly low effusion rate. As the dike rises from the mantle source region, gas is
364 exsolved (e.g., Wilson & Head, 2003; Rutherford et al., 2017) and concentrated in the dike tip,
365 below which is bubble-rich magmatic foam, both overlying the rising magma in the remainder of
366 the dike. During Phase 1, the dike penetrates to the surface vacuum, and the gas and magmatic
367 foam in the upper part of the dike explosively vent to the surface. In high-effusion rate eruptions
368 (Figure 11A), the explosion accompanying the transient gas release phase is rapidly followed by
369 the Phase 2 eruptive phase as magma surges onto the surface. In the much lower-volume and
370 lower-effusion rate-case of the small volume end of small shield volcanoes, the Phase 1
371 explosive venting at the top of the dike leaves a void into which the brecciated country rock of
372 the dike wall can collapse (Figure 11B). As the magma below the evacuated gas and foam at the

373 top of the dike then continues to rise in the dike toward the surface, the rise rate is sufficiently
374 low (less than 5 m/s) that Phases 2 and 3 do not occur in a manner similar to that in large-volume
375 eruptions. Instead, in a highly abbreviated Phase 2-3, the relatively degassed magma in the top of
376 the dike rises into the newly formed collapsed pit and extrudes out onto the surface to form the
377 initial layers of a small shield. As the magma rise speed decreases to less than ~ 1 m/s, Phase 4 is
378 initiated. Due to the very slow magma rise speed, ascending bubbles of CO released at great
379 depth (Rutherford et al., 2017) have sufficient time to form, expand, rise and coalesce into slugs.
380 Strombolian activity (bursting of coalesced gas slugs at the top of the lava lake; Blackburn et al.,
381 1976; Ripepe et al., 2008) will be the result. However, beneath the undisturbed parts of the lava
382 lake, relatively soluble and therefore shallow-nucleating water and sulfur compounds (e.g.,
383 Rutherford et al., 2017; Head & Wilson, 2017) will have had time to exsolve, leading to very
384 high vesicularity.

385 Four factors are important in the waning stages of a typical small-volume, small-effusion
386 rate eruption: 1) magma rise-rate, already low due to the small volume of the eruption, continues
387 to decrease due to the lack of additional deeper magma in the dike, 2) the low rise-rate
388 maximizes gas exsolution in the remaining magma in the dike, causing volume expansion, 3)
389 elastic forces initially holding the dike open begin to relax, contributing to closure of the dike,
390 and 4) magma lining the walls of the dike conductively cools, further narrowing the dike and
391 decreasing the remaining dike volume. Although these processes act at different rates, the net
392 balance of forces tends to drive the lava lake surface upward in a piston-like manner; the very
393 bubble-rich/vesicular magma in the lava pond and dike below are thus forced upward, filling and
394 potentially overtopping the lake, and causing effusion of very vesicular lava out onto the small
395 shield volcano rims and flanks. This type of late stage behavior is well documented in terrestrial
396 small shields, pit craters and low-volume eruptions, and can result in multiple phases of lava lake
397 rise and fall (e.g., Tilling, 1987; Tilling et al., 1987; Wolfe et al., 1987).

398 Continuing loss of volume from 1) dike-magma supply exhaustion, 2) dike solidification
399 and 3) loss of gas volume from strombolian activity in the lava lake, results in the final recession
400 of the lava lake floor down into the pit crater interior. In terrestrial small shield volcanoes and pit
401 craters, the eruption comes to an end when the thermal boundary layer at the lava lake surface
402 solidifies to a thickness sufficient to cause rising magmatic slugs to collect below the lava lake
403 floor, instead of disrupting the surface in strombolian activity (e.g., Blackburn et al., 1976).

404 On the Moon, the low gravity and absence of atmosphere lead to a low overburden pressure
405 resulting in a different behavior from that of typical terrestrial eruptions. For a given magma
406 volatile content, lunar lava lakes will have a proportionally greater amount of bubbles forming
407 below the solid surface. As the lunar lava lake magma continues to cool, second boiling causes
408 further release of remaining magmatic volatiles (Wilson et al., 2019), adding to the total volume
409 of gas. The final products from all of the gas exsolving from the magma remaining in the top of
410 the dike and lava lake build up below the thickening lava lake floor layer, collecting as 1) gas
411 void space (rising gas slugs trapped beneath the solidified floor), 2) very vesicular magmas
412 (rising gas bubbles and bubble-rich magma) and 3) magmatic foams (where the vesicle content
413 exceeds $\sim 75\%$ of the volume). Models of the effects of these unusual lunar environmental
414 conditions in the last stages of enhanced magmatic volatile collection below a lava lake suggest
415 that lava lake floor flexure and cracking can result in the extrusion of magmatic foams onto the
416 surface of the lava lake (Wilson & Head, 2017a), a process unknown on the Earth.

417 The final stage of the dike emplacement event occurs at the end of Phase 4 activity, when

418 the lava lake and underlying dike cool and solidify, a process lasting up to several years. During
419 this period, the remaining cooling magma in the top of the dike and lava lake will undergo an
420 ~10% volume reduction due to solidification, and the lava lake floor will adjust to this volume
421 decrease by sagging and lowering accordingly.

422 The fate of any highly bubble-rich/vesicular magma that is forced up and out of the lava
423 lake and flows out onto the small shield volcano flanks is predicted to be the following. First,
424 plates of the partly solidified lava lake floor will be rafted out onto the small shield rim and
425 flanks. Secondly, the upper surfaces of the extremely vesicular flows will undergo a mild
426 explosive activity into the overlying vacuum to form a meters-thick layer of “auto-regolith”
427 (Head & Wilson, 2019), a carpet of explosively ruptured bubble wall fragments and glass shards
428 that protects the underlying flow from further explosive disruption (Wilson et al., 2019). As the
429 very bubble-rich/vesicular lava flows on the flanks of the shield continue to cool below the auto-
430 regolith layer, second boiling causes the exsolved bubbles and foams to continue to form, grow,
431 and to migrate laterally and rise vertically; shear from final flow emplacement and cooling can
432 locally break down bubbles and form voids beneath the cooling and thickening auto-regolith and
433 solidified flow surface. As the flank flows continue to cool, second boiling of the cooling magma
434 at the base of the flow is predicted to cause new gas exsolution, bubble growth, flow inflation
435 and migration of bubble and foam-rich magma laterally and vertically in the flow (e.g., Wilson et
436 al., 2019). This late-stage process adds to the volume of very vesicular foam and gas pockets
437 below the cooling and thickening flow surface. Final solidification of flank flows is predicted to
438 result in a three-layer stratigraphy (Wilson et al., 2019; Head & Wilson, 2019): a) an upper,
439 meters-thick, auto-regolith layer of glassy bubble-wall shards above a lower, welded, pyroclast
440 layer, grading down into b) a medial, many meters-thick, highly vesicular-foamy layer with
441 distributed linear and circular pockets of voids formed by bubble-foam collapse and gas
442 migration and collection, and c) a lower layer of solidified degassed magma chilled against the
443 underlying pre-eruption surface.

444 These theoretical analyses of the nature of low-volume, low-effusion rate small shield
445 volcano eruptions on the Moon (Figure 11B) (e.g., Wilson & Head, 2017a, 2018, 2019; Head &
446 Wilson, 2017; Rutherford et al, 2017; Wilson & Head., 2018) provide a framework of
447 predictions for assessing and interpreting the nature, structure, morphology and history of the
448 Cauchy 5 small shield volcano.

449 **4. Synthesis of Cauchy 5 Small Shield Volcano Emplacement History and Setting for Type** 450 **1 and 2 IMPs**

451 We now revisit the major characteristics of the Cauchy 5 small shield volcano outlined in
452 Section 2 (illustrated in Figures 2-10 and S2-3) and assess these in the context of the models of
453 the generation, ascent and eruption of lunar magmas, and the several phases in their
454 emplacement, described above (Figure 11B), leading to the following interpreted steps in the
455 geologic history of the Cauchy 5 small shield volcano and its associated Type 1 and Type 2
456 IMPs (Figures 12-14).

457 *1) Formation and upward propagation of magma-filled, convex-upward crack and dike*
458 *from the source region in the lunar mantle:* The volume of magma in the dike is small relative to
459 that in typical mare basalt eruptions. Magma overpressurization and the mantle-melt density
460 contrast cause the dike to rise buoyantly into the overlying less-dense anorthositic crust where
461 the change to negative buoyancy results in a decrease in propagation velocity (Figure 12a). As

462 the dike rises from the source region, gas exsolves in the propagating low-pressure zone in the
463 crack forming the tip of the dike (e.g., Wilson & Head, 2003), and collects as free gas in the
464 upper part of the dike and as a zone of gas bubbles in the region below the gas and above the
465 bulk of the magma.

466 *2) Initial arrival and penetration to the surface of the convex-upward, WNW-trending dike*
467 *from depth in the mantle: Eruption Phase 1:* As the relatively slowly rising dike decreases
468 further in propagation velocity as more of it enters the low-density crust, the dike tip reaches the
469 lunar surface and erupts into the vacuum, resulting in explosive venting of the gas and magmatic
470 foam in the top of the dike (Figures 11b and 12b). This gas and explosively disrupted foam of the
471 Cauchy 5 eruption lasts only a few minutes; disrupted foam bubble wall pyroclasts are very
472 widely dispersed in the region surrounding the vent. The explosive venting creates a large void
473 space in the slowly rising upper few hundred meters of the dike; dike wall material shattered by
474 the explosive venting collapses into the void to create an elongate ($\sim 0.75 \times 2$ km) surface
475 collapse crater along the strike of the dike (Figure 13a).

476 *3) Slow rise of relatively degassed magma in the top of the dike: Abbreviated Eruption*
477 *Phase 2/3:* As the magma continues to rise in the dike, the largely degassed magma (previously
478 below the now-vented gas and magmatic foam dike tip area; Figure 12a) slowly rises and
479 extrudes out onto the surface, forming the initial layers of the small shield as it builds up around
480 the vent (Figure 12c). Predicted low magma rise speeds and volume fluxes support the
481 interpretation that this initial phase will consist of cooling-limited flows (Head & Wilson, 2017)
482 extending a few kilometers radially away from the vent (Figure 13b). The low magma volumes
483 and rise rates compared with more typical mare basalt eruptions, and the largely degassed nature
484 of the magma, result in extremely abbreviated eruption Phases 2 and 3 (Figure 11B).

485 *4) Strombolian activity-vesicular flow eruption phase: Phase 4:* Newly arrived gas-
486 containing magma from below the gas-depleted upper part of the dike enters the low-
487 overburden-pressure upper several kilometers of the dike, exsolving gas as it rises (Rutherford et
488 al., 2017) (Figure 12d). The very low magma rise rate maximizes the amount of gas exsolution,
489 particularly of CO released at great depths, bubble rise, growth and coalescence, and causes
490 episodic strombolian activity (Blackburn et al., 1976) in the summit pit crater. The cooling
491 thermal boundary layer at the top of the lava lake floor begins to form and stabilize, but is
492 disrupted by the rising and bursting gas slugs of the strombolian activity.

493 *5) Lava lake inflation and overflow: Phase 4:* As the magma rise rate in the dike at depth
494 decreases toward zero, signaling the final stages of the eruption (Figure 11B), other forces come
495 into play to cause fluctuation of the lava lake level. A combination of a) increasing dike magma
496 volume due to shallow-release gas bubble formation causing magma expansion, and b)
497 relaxation of elastic forces initially holding the dike open, force the extremely bubble-rich
498 magma up into the pit crater, over the rim and onto the flanks of the nascent small shield volcano
499 (Figures 12e and 13c).

500 *6) Emplacement of very highly vesicular/foamy flanking flows: Phase 4:* In this latter stage
501 of Phase 4, the lava lake floor rises and lava spills out over the rim of the small shield, producing
502 a second stage of flanking flows (Figure 12e). In contrast to the initial stage of largely volatile
503 depleted flows, the emplaced magma is now composed of the extremely bubble-rich foamy lava
504 that has collected in the lava lake below the cooling crust. Portions of the cooled lava lake floor
505 crust are disrupted and emplaced on the shield flanks. The newly erupted upper layers of the

506 extremely vesicular/foamy lava flows are exposed to the lunar surface vacuum. They decompress
507 explosively to form a meters-thick layer of “auto-regolith”, a carpet of popped bubble wall
508 fragments and glass shards (Head & Wilson, 2019). The unusual remote sensing properties of the
509 Cauchy 5 flanking flow surfaces (anomalously finer grained, block poor; Figures 9 and S4) are
510 attributed to the glassy auto-regolith layer produced by this explosive decompression of the
511 upper vesicle-rich layer of the extruded flows as they encounter the surface vacuum. The
512 relatively optically immature and blockier nature of the flanking Type 2 IMP pit walls and floors
513 (Figures 8 and 9) are interpreted to be due to post-flow-emplacement/cooling impact crater
514 events; these cause collapse of voids of various scales and shapes, and different ages (consistent
515 with the observed optical maturity variations), exposing fresh, more coherent material from the
516 underlying parts of the flow.

517 *7) Termination of the eruption and recession of the lava lake floor into the pit crater:* As the
518 magma rise rate in the dike decreases to zero, signaling the end of the eruption, continued
519 degassing of magma in the lava lake decreases the total volume of magma in the dike and lava
520 lake, causing recession (Figure 12f) and magma withdrawal into the pit crater, leading ultimately
521 to stabilization of the lava lake floor. This is enhanced by the volume reduction of the magma in
522 the deeper parts of the dike as it cools and solidifies. The lava lake surface crust continues to
523 thicken, further suppressing the strombolian eruption bursts caused by rising magmatic gas slugs
524 (Figure 12g). These bursts eventually cease as all of the deep-sourced gas is exhausted.

525 *8) Drainback of portions of the rim lavas into the crater interior:* As the lava lake floor
526 deflates and subsides into the pit crater, portions of the still-cooling lava flow on the rim drain
527 back into the pit crater interior (Figure 13d), leaving islands of cooled lava and auto-regolith,
528 interspersed with regions where the chilled upper layer of the flow has drained back into the pit
529 crater, exposing the very bubble-rich/vesicular parts of the flow (Figures 5-7). This leads to
530 unusual patterns and topography of the exposed and bubble/foam-rich interior of the flow, and
531 possible degassing of foams to form mounds and depressions.

532 *9) Eruption aftermath: Pit crater interior:* In this post-eruption period, the lava lake in the
533 pit crater interior begins to undergo final cooling, degassing and solidification (Figure 12h). The
534 upper cooling thermal boundary layer (the macro and micro-vesicular lava lake floor) continues
535 to thicken and solidify, inhibiting further strombolian activity and gas loss to the surface. The
536 most recently arrived magma in the top of the dike continues to degas under the thickening lava
537 lake floor, exsolving significant quantities of gas bubbles that rise and collect as a magmatic
538 foam below the lava lake crust. As the lava lake cools further, second boiling (Wilson et al.,
539 2019) contributes additional volatiles. In contrast to terrestrial eruptions at this stage, the low
540 lunar gravity and low overburden pressure together favor extensive gas production, bubble
541 growth and foam development in the lava lake. This excess volume can cause flexing and
542 fracturing of the cooling and thickening lava lake floor crust. Models of this configuration in
543 other pit craters predict that this flexing and cracking can result in the extrusion of portions of the
544 underlying magmatic foams out onto the lava lake floor to produce magmatic foam mounds and
545 coalesced deposits (Wilson & Head, 2017a; Qiao et al., 2018, 2019a) (Figures 12h and 13e).
546 Evacuation of foams to the surface can result in additional subsidence and/or production of large
547 void spaces below the flexing thermal boundary layer, depending on its local thickness and
548 rheology. Final solidification of the lava lake will cause additional subsidence in the lava lake
549 interior (Figure 12i).

550 *10) Predicted final substrate target properties: Pit crater interior:* On the basis of this
551 interpreted Cauchy 5 eruption history (Figures 12a-i and 13a-e), following the end of the
552 eruption, the interior of the pit crater should be characterized by a cross-section (Figure 14a)
553 consisting of: 1) a solidified very highly macro- and micro-vesicular boundary layer of the lava
554 lake floor, superposed by coalesced extrusions of magmatic foam (topped by a meters-thick layer
555 of auto-regolith). 2) An underlying layer of coalesced bubbles and foams that have risen in the
556 lava lake and solidified beneath the lava lake floor. Bubbles and foams should dominate the top
557 of this underlying layer, producing extreme macro and micro-vesicularity. This layer should also
558 contain large meters-scale voids formed from gas slugs that have risen in the dike and lake and
559 become trapped below the lava lake crust. Additional large voids might be anticipated from
560 space left by foams leaking to the surface through flexing and cracking of the lava lake surface
561 layer. 3) Lower layers of progressively degassed lavas from which exsolved bubbles have risen
562 upward in the cooling lava lake. This distinctive substrate (Figure 14a) lies in stark contrast to
563 the initial solid lava substrate predicted to be typical of nominal Phase 2 distal lava flows (Figure
564 11A) representing the majority of the lunar mare surfaces (Wilson & Head, 2017b; Head &
565 Wilson 2017, 2019).

566 *11) Eruption aftermath: Flanking bubble-rich/vesicular flows:* At the end of the eruption,
567 the very bubble-rich/vesicular flows on the flanks of the volcano continue to cool (Figure 14b).
568 Exsolved bubbles and foams continue to migrate laterally and rise vertically; shear from the final
569 flow emplacement and cooling can locally break down bubbles and form voids beneath the
570 cooling and thickening auto-regolith and solidified flow surface. As the flank flows continue to
571 cool, second boiling (Wilson et al., 2019) of the cooling magma toward the base of the flow
572 causes new gas exsolution, bubble growth, flow inflation and migration of bubble and foam-rich
573 magma laterally and vertically in the flow, adding to the very vesicular foam and gas pockets
574 below the cooling and thickening flow surface. If pressure in local gas pockets and cavities
575 exceeds the overburden pressure of overlying auto-regolith layer and the evolving mechanical
576 strength of the welded pyroclast layer at the base of the auto-regolith layer, there is the potential
577 for formation of local explosion craters. This final inflation activity should also contribute to the
578 hummocky topography of the final flow surface (Figure 3d).

579 *12) Predicted final substrate target properties: Flanking bubble-rich/vesicular flows:* Final
580 solidification of the flank flows is predicted to result in a three-layer stratigraphy (Figure 14b): a)
581 an upper, meters-thick, auto-regolith layer of glassy bubble-wall shards above a lower, welded,
582 pyroclast layer, grading down into b) a medial, many meters-thick, highly vesicular-foamy layer
583 with distributed linear and circular pockets of voids formed by bubble-foam collapse and gas
584 migration and collection, and c) a lower layer of solidified degassed magma chilled against the
585 underlying flow.

586 *13) Subsequent history of Cauchy 5 small shield volcano:* The interpreted multi-stage
587 eruption history of the Cauchy 5 small shield volcano outlined above (Figures 12a-i and 13a-e)
588 sets the stage for its post-solidification geologic history, consisting largely of superposed impact
589 cratering events and regolith development and thickening.

590 We now use this synthesis as a basis for discussion of several outstanding issues, including
591 1) the relationship between the IMPs on the pit crater floor and those on the shield volcano rim
592 and flank, 2) the nature and evolution of the impact generated regolith, 3) the influence of the
593 substrate on the superposed impact crater population and 4) the estimated absolute age of the
594 emplacement of the Cauchy 5 small shield volcano.

595 **5. Discussion**

596 **5.1. Insights into the Origin of IMPs: Cauchy 5 Small Shield Volcano as a Guide**

597 We now proceed to compare 1) the nature of the substrate on the Cauchy 5 pit crater floor
598 (Figure 14a) and the small-shield flank (Figure 14b) and 2) the processes of impact cratering and
599 regolith formation subsequent to edifice formation and cooling, in order to try to account for the
600 major characteristics of the Type 1 and Type 2 IMPs. For the pit crater floor, these characteristics
601 are: 1) the rough and relatively immature nature of portions of the floor, 2) the meniscus-like
602 morphology and optically relatively more mature properties of the extensive lower albedo
603 mound-like areas, and 3) the CSFD-derived age of ~58 Ma. For the small shield flanks these
604 characteristics are: 1) the size, shape, depth and areal distribution of the pits, and their relative,
605 but variable, optical immaturity, 2) the fine-grained, block-poor nature, topography and
606 morphology of the lower albedo shield flanks in which the pits are contained, and 3) the ~160
607 Ma CSFD age for the shield flanks, compared with the >3000 Ma age of the surrounding maria.
608 The Type 1 IMP mound and floor deposits in the summit pit crater are interpreted to have
609 formed during the final phase of the emplacement of the edifice. The Type 2 small pit IMPs on
610 the shield volcano flanks could have formed in part from late-emplacement-stage explosion
611 craters, but the majority are interpreted to have formed subsequently, as the flanking void-rich
612 flows were subjected to impact cratering at a variety of scales and ages.

613 **5.2. Nature of the Initial Substrate at Cauchy 5 Small Shield Volcano and Influence on the** 614 **Formation of Regolith and Type 2 IMPs**

615 Exploration and characterization of the lunar regolith overlying mare basalt lava flows by
616 the Apollo 11, 12, 15 and 17 missions showed that it consists largely of a soil layer composed of
617 mechanically fragmented solid lava flows (McKay et al., 1991; Lucey et al., 2006). Initial impact
618 fragmentation produces optically immature bedrock blocks and rocky soils (Figure 15);
619 subsequent impact events at all scales reduce the grain size, increase the proportion of glassy
620 agglutinates, thicken the regolith layer and create an optically more mature surface layer (Lucey
621 et al., 2006). As the regolith thickness increases, impact craters that penetrate through the
622 regolith into the underlying solid basalt substrate become more infrequent. The morphology of
623 these larger crater interiors and the occurrences of blocks in fresh craters can be used to estimate
624 the thickness of the regolith layer (e.g., Quaide and Oberbeck, 1968; Qiao et al., 2016), and
625 radiometric dating of the basalt lava flows at the Apollo landing sites can then provide an
626 estimate of regolith growth rates that can be extrapolated to unsampled mare areas using crater
627 morphology (e.g., Di et al., 2016).

628 These estimates of thickness and characteristics are, however, predicated on the assumption
629 that the initial substrate on which the impact generated regolith is developed consists of solid
630 basaltic lava flows (Figure 15), a good assumption for the geologic setting of the Apollo 11, 12,
631 15 and 17 landing sites. On the basis of our analysis and characterization of the Cauchy 5 small
632 shield volcano Phase 4 volatile-rich magma behavior, the initial, post-emplacement/cooling
633 Cauchy 5 pit floor and flank deposits (Figures 14a and b) are significantly different from the
634 typical solid basalt flow surfaces on which regolith developed at the Apollo mare landing sites
635 (Figure 15).

636 How will these differences influence the development of regolith? The partitioning of
637 energy in impact cratering events provides a framework for addressing this question (Gault et al.,

638 1968). In solid mare basalt substrates (Figure 15), the kinetic energy of impact is partitioned
639 primarily into rock fracturing, fragmentation and lateral ejection; seismic energy is efficiently
640 radiated away from the sub-impact point due to the solid nature of the substrate. As regolith
641 thickness grows, the ratio of energy expended in fracturing/fragmentation relative to ejection
642 decreases and seismic energy is attenuated (relative to bedrock) by the increasing thickness of
643 the more porous regolith.

644 In contrast, impact energy partitioning in very porous, vesicular, foamy and void-rich
645 substrates (Figure 14) is predicted to be very different (e.g., Kadono, 1999; Flynn et al., 2015;
646 Okamoto & Nakamura, 2017; Housen et al, 2018; Head & Ivanov, 2019; Ivanov & Head, 2019).
647 A significant percentage of the impact kinetic energy is now partitioned into crushing and
648 collapse of the vesicles and voids, favoring vertical penetration of the projectile and vertical
649 growth of the cavity, rather than lateral ejection (the well-known aerogel effect). Impact craters
650 in vesicular/foamy substrates are thus predicted to be deeper and less wide than analogous events
651 in a solid basaltic substrate; corresponding subdued lateral emplacement of ejecta is also
652 predicted. In cases where larger subsurface voids exist (Figure 14) (see also Robinson et al.,
653 2012), superposed impacts are predicted to cause fragmentation and collapse of layers overlying
654 the voids, and exposure of fresh materials in the collapse-crater walls. Seismic energy
655 attenuation in vesicular/foamy substrates is maximized, due to the high abundance of pore space.

656 Application of these principles to the Cauchy 5 small shield volcano deposits (Figure 14)
657 results in the following interpretations. Superposed impact crater morphology and morphometry,
658 as well as regolith buildup, are predicted to be significantly influenced by the multi-scale and
659 abundant void space (Figure 16) (Head & Ivanov, 2019; Ivanov & Head, 2019). Energy
660 partitioning will favor production of relatively smaller, irregularly-shaped deeper craters, less
661 lateral ejection, and the drainage of fragmented material down into the underlying void spaces
662 below and adjacent to the crater. Impact-induced seismic shaking in the vicinity of the event
663 from this and other impact events (Yasui et al., 2015; Qiao et al, 2017) will enhance the seismic-
664 sifting and drainage of fragmental down into the subsurface void space, helping to perpetuate the
665 optical immaturity of the newly exposed rocky material. These unusual properties of superposed
666 crater formation, and regolith evolution and drainage, may render some impact craters difficult to
667 recognize.

668 The *pit crater floor rough unit* is predicted to be superposed by coalesced extrusions of
669 *magmatic foam* dominated by abundant micro-vesicularity (Figure 14a) and an upper layer of
670 explosively disrupted glassy vesicle walls that builds a meters-thick auto-regolith layer and
671 inhibits the further disruption of the underlying extruded foams (Head & Wilson, 2019). The
672 enhanced viscosity of the extruded foams results in a meniscus effect at the mound margins, in
673 contrast to the underlying rough lava lake floor substrate. Craters subsequently superposed on the
674 mounds (Figure 16a) are predicted to first encounter the meters-thick auto-regolith layer and then
675 the underlying foam layer, resulting in variable energy partitioning and potentially resulting in
676 funnel-shaped craters.

677 These distinctive substrates (Figure 14a) lie in stark contrast to the initial solid lava
678 substrate predicted to be typical of nominal Phase 2 distal lava flows representing the majority of
679 the lunar mare surfaces (Langevin & Arnold, 1977; Hörz, 1977; Wilcox et al., 2005) and are not
680 readily interpretable in the context of traditional solid bedrock regolith growth models (Figure
681 15). Instead, these combined considerations of initial substrate characteristics and the effects on
682 superposed impacts and regolith buildup predict that: 1) the *rough floor unit* should have unusual

683 superposed craters (Figure 16b), regolith buildup will be inhibited due to seismic sifting and
684 drainage, and optical immaturity should be prolonged for much greater durations due to the
685 continued exposure of fresh rock material by regolith drainage; 2) the *mound unit* should begin
686 with an optically more mature auto-regolith layer dominated by glassy bubble wall fragments, an
687 underlying magmatic foam layer overlying the crater floor, and unusually shaped superposed
688 impact craters whose properties are dominated by vertical crushing, rather than lateral ejection,
689 and more rapid degradation of craters than on normal solid mare basalt regoliths.

690 The predicted characteristics of the *bubble-rich/vesicular shield flanking flow units* (Figure
691 14b) provides an additional contrast to both the pit crater floor (Figure 14a) and the solid mare
692 basalt substrate (Figure 15) predictions. Impact craters forming in the three-layer stratigraphy
693 (Figure 14b) will initially encounter an upper, meters-thick, auto-regolith layer of glassy bubble-
694 wall shards above a lower, welded, pyroclast layer. This grades down into a medial, meters-
695 thick, highly vesicular-foamy layer with distributed linear and circular pockets of voids formed
696 by bubble-foam collapse and gas migration and collection from initial flow emplacement and
697 second boiling during solidification. Small superposed impacts (Figure 16c) will create relatively
698 subdued craters in the auto-regolith layer that will degrade rapidly. Larger impact events will
699 penetrate through this fragmental layer, encountering a layer of laterally varying porosity.
700 Response to these cratering events (Figure 16c) is predicted to range from: 1) impact-induced
701 mechanical collapse of surface material into underlying layer void space, forming pits with a
702 relatively immature deposit on the floor and exposing adjacent fresh layers in the pit walls (e.g.,
703 Figure 17a); 2) shock-induced shattering of bubble and foam walls and collapse of overlying
704 layers producing depressions and pits that should be highly irregular in shape (e.g., Figure 17b)
705 due to a) heterogeneities in bubble size and spatial distribution and b) variations in shock wave
706 magnitudes and symmetries; 3) a variety of craters with non-traditional morphologies,
707 degradation states and morphometries due to lateral and vertical variations in size and
708 distribution of layer pore space and the effects on energy partitioning (e.g., Figure 17c); and 4)
709 craters formed in rafted lava plates and less vesicular parts of the flank flow that are predicted to
710 be more similar to those formed in solid bedrock with a modest thickness of regolith (the auto-
711 regolith in the case of the flank flows). Even larger impact events will penetrate through the
712 entire flanking flow into the underlying solid basalt shield and regional mare substrate deposits.
713 Intermediate to larger-scale craters that penetrate through the porous layer are predicted to
714 expose the porous layer in the upper part of their walls (e.g., Figure 17d). Examples of this
715 diversity of predicted flanking flow morphologies observed at Cauchy 5 are shown in Figures
716 16c and 17.

717 In this scenario, the majority of the pits observed on the Cauchy 5 shield flanks would form
718 throughout the post-emplacement history of the flank flows. Thus, the walls and floors of the pits
719 are expected to show a range of optical maturity related to the time since their formation and the
720 reduction in the initially steep slopes of the pit walls. The wide range of pit optical maturity
721 levels observed supports this hypothesis and suggests that the vast majority of the pits did not
722 form at the time of flank flow emplacement. Indeed, few pits are observed that have maturity
723 levels indistinguishable from those of the adjacent inter-pit regolith surface (Figure 9).

724 **6. Summary and Conclusions**

725 We combined the predictions of a lava flow emplacement model and observation of the
726 characteristics of Cauchy 5 to interpret: 1) the *elongate pit crater* to be the consequence of the

727 initial venting of the dike magma to the surface and collapse of the top of the dike and adjacent
728 substrate into the resulting void, 2) the *low volume of the shield* to be related to the low-volume,
729 low-rise-rate nature of the dike emplacement event, 3) the *flank flows containing small Type 2*
730 *IMPs* to be related to the overtopping of gas-bubble-rich magma from the lava lake onto the
731 small shield flanks, and formation and migration of volatiles during bubble-rich/vesicular flow
732 emplacement and its subsequent cooling, second boiling, and bubble migration to form gas-rich
733 pockets and voids that collapsed due to subsequent impacts, 4) the *mound-like unit on the pit*
734 *crater floor* to be related to the final stages of the activity in the lava lake pit crater interior: the
735 cooling thermal boundary layer of the lava lake floor, the formation of magmatic foams below
736 this layer, and the cracking and extrusion of foams onto the solidifying lava lake floor.

737 The unusual optical and radar remote sensing properties of the Cauchy 5 flanking flow
738 surfaces (anomalously finer grained, block poor) are attributed to the glassy auto-regolith layer
739 produced by the explosive decompression of the upper vesicle-rich layer of the extruded flows as
740 they encounter the surface vacuum. The relatively optically immature and blockier nature of the
741 flanking Type 2 IMP pit walls and floors are interpreted to be due primarily to subsequent impact
742 crater events in the post-flow emplacement/cooling; these cause collapse of voids of different
743 scales and shapes and different ages, exposing fresh, more coherent materials from the
744 underlying parts of the flow.

745 We conclude that this small-volume, low-effusion-rate eruption scenario may help explain
746 the relationship between the characteristics and mode of formation of Type 1 (large) IMPs (pit
747 crater floor evolution and extrusion of foams) and Type 2 (small) IMPs (very bubble-
748 rich/vesicular flank flows and the formation and evolution of void space within the flows). The
749 unusual hybrid association of Type 1 and Type 2 IMPs at Cauchy 5 is thought to be related to its
750 small size, caused by its low-volume, low-effusion-rate eruption, and the suppression of the
751 volumetrically significant Phases 2 and 3 characteristic of larger eruptions.

752 Remaining incompletely explained are: 1) the superposed CSFD and absolute model ages
753 interpreted to represent an age of ~58 Ma for the pit crater and ~160 Ma for the flank flows, both
754 ages seemingly inconsistent with the age of regional surrounding flows (>3000 Ma); 2) the
755 morphologically crisp and optically immature aspects of IMPs, and 3) why the small Type 2
756 IMPs on the flanks of Cauchy 5 are smaller (~115 m) than the Type 2 IMPs in the rest of the
757 population elsewhere on the Moon (~275 m average length).

758 We speculate that the discrepancy in CSFD-derived ages may be due to substrate target
759 properties: the very porous nature of the pit crater floor substrate and the auto-regolith on the
760 shield flanks. Kinetic energy partitioning of projectiles impacting into the vesicle-foam-void-rich
761 substrate will favor the vertical crushing and collapse of voids rather than brittle deformation and
762 lateral ejection; these factors influence both the resulting size of craters (smaller, thus net
763 younger CSFD ages) and the degradation state (changing the fundamental nature of the
764 diffusion-dominated landscape degradation models (e.g., Fassett & Thomson, 2014)). Craters
765 formed in the incoherent upper layer of the auto-regolith-covered flank flows will degrade faster
766 and thus not be represented in CSFD-derived ages. Although a conclusive link to these factors
767 has yet to be demonstrated, we infer that these observations favor an age for Cauchy 5 small
768 shield volcano formation closer to that of the surrounding maria (>3 Ga) than to formation in the
769 last several tens of millions of years.

770 Finally, the occurrence of Type 2 (small) IMPs at Cauchy 5 provides evidence that other
771 Type 2 IMPs elsewhere on the Moon may be linked to Phase 4 lava flow emplacement, with its
772 relatively enhanced volatile content and vesicle/foam/void formation. We speculate that the
773 larger size of Type 2 IMPs in the dozens of occurrences scattered across the lunar maria (average
774 length ~275 m compared with ~115 m for Cauchy 5 flanks) may be explained by Phase 4 activity
775 in the much thicker inflated bubble-rich/vesicular flows typical of more common large-volume
776 eruptions. Phase 4 lava flow emplacement, and subsequent inflation and second boiling in much
777 thicker flows, should favor development of locally larger void spaces and their subsequent
778 collapse by impact events.

779 These conjectures can be tested by further analysis of the IMP population, and experimental
780 and observational studies of the nature of impact cratering into porous and incoherent media, and
781 the subsequent crater degradation.

782 **Acknowledgments**

783 This work is partly supported by the National Natural Science Foundation of China (Nos.
784 41703063, 11941001 and 41972322), a Pre-research Project on Civil Aerospace Technologies
785 No. D020205 funded by CNSA and Qilu (Tang) Young Scholars Program of Shandong
786 University, Weihai (2015WHWLJH14). JWH gratefully acknowledges financial support from
787 the NASA Lunar Reconnaissance Orbiter (LRO) Mission, Lunar Orbiter Laser Altimeter
788 (LOLA) Experiment Team (Grants NNX11AK29G and NNX13AO77G) and the NASA Solar
789 System Exploration Research Virtual Institute (SSERVI) grant for Evolution and Environment of
790 Exploration Destinations under cooperative agreement number NNA14AB01A at Brown
791 University. LW thanks the Leverhulme Trust for support through an Emeritus Fellowship. All
792 original LROC data can be retrieved from the LROC PDS archive
793 (<http://wms.lroc.asu.edu/lroc/search>), all Arecibo data can be found in the NASA Planetary Data
794 System Geosciences Node (<https://pds-geosciences.wustl.edu/missions/sband/index.htm>), all
795 original Kaguya/SELENE Multiband Imager data are archived at SELENE Data Archive
796 (<https://darts.isas.jaxa.jp/planet/pdap/selene/>). The pit measurement and crater count data are
797 accessible at http://www.planetary.brown.edu/html_pages/data.htm

798 **References**

- 799 Barker, M. K., Mazarico, E., Neumann, G. A., Zuber, M. T., Haruyama, J., & Smith, D. E.
800 (2016). A new lunar digital elevation model from the Lunar Orbiter Laser Altimeter and
801 SELENE Terrain Camera. *Icarus*, 273, 346-355.
802 <http://dx.doi.org/10.1016/j.icarus.2015.07.039>
- 803 Bennett, K. A., Horgan, B. H. N., Bell, J. F., III, Meyer, H. M., & Robinson, M. S. (2015). Moon
804 Mineralogy Mapper investigation of the Ina irregular mare patch. *46th Lunar and Planetary
805 Science Conference*, Lunar and Planetary Institute, The Woodlands, Texas, abstract #2646.
- 806 Blackburn, E. A., Wilson, L. & Sparks, R. S. J. (1976) Mechanisms and dynamics of strombolian
807 activity, *Journal of the Geological Society*, 132, 429-440.
808 <https://doi.org/10.1144/gsjgs.132.4.0429>
- 809 Braden, S. E., Stopar, J. D., Robinson, M. S., Lawrence, S. J., van der Bogert, C. H., &
810 Hiesinger, H. (2014), Evidence for basaltic volcanism on the Moon within the past 100 million
811 years. *Nature Geoscience*, 7(11), 787-791. <https://doi.org/10.1038/ngeo2252>

- 812 Carter, L. M., Hawke, B. R., Garry, W. B., Campbell, B. A., Giguere, T. A., & Bussey, D. B. J.
813 (2013). Radar observations of lunar hollow terrain. *44th Lunar and Planetary Science*
814 *Conference*, Lunar and Planetary Institute, The Woodlands, Texas, abstract #2146.
- 815 Campbell, B. A., Carter, L. M., Campbell, D. B., Nolan, M., Chandler, J., Ghent, R. R., et al.
816 (2010). Earth-based 12.6-cm wavelength radar mapping of the Moon: New views of impact
817 melt distribution and mare physical properties. *Icarus*, 208(2), 565-573.
818 <https://doi.org/10.1016/j.icarus.2010.03.011>
- 819 Crater Analysis Techniques Working Group (1979). Standard techniques for presentation and
820 analysis of crater size-frequency data. *Icarus*, 37(2), 467-474. [https://doi.org/10.1016/0019-](https://doi.org/10.1016/0019-1035(79)90009-5)
821 [1035\(79\)90009-5](https://doi.org/10.1016/0019-1035(79)90009-5)
- 822 Di, K., Sun, S., Yue, Z., & Liu, B. (2016). Lunar regolith thickness determination from 3D
823 morphology of small fresh craters. *Icarus*, 267, 12-23.
824 <https://doi.org/10.1016/j.icarus.2015.12.013>
- 825 Elder, C. M., Hayne, P. O., Bandfield, J. L., Ghent, R. R., Williams, J. P., Donaldson Hanna, K.
826 L., & Paige, D. A. (2017). Young lunar volcanic features: Thermophysical properties and
827 formation. *Icarus*, 290, 224-237. <https://doi.org/10.1016/j.icarus.2017.03.004>
- 828 Fassett, C. I., & Thomson, B. J. (2014). Crater degradation on the lunar maria: Topographic
829 diffusion and the rate of erosion on the Moon. *Journal of Geophysical Research: Planets*, 119,
830 2255 – 2271. <https://doi.org/10.1002/2014je004698>
- 831 Fassett, C. I. (2016). Analysis of impact crater populations and the geochronology of planetary
832 surfaces in the inner solar system. *Journal of Geophysical Research: Planets*, 121(10), 1900-
833 1926. <https://doi.org/10.1002/2016JE005094>
- 834 Flynn, G. J., Durda, D. D., Patmore, E. B., Clayton, A. N., Jack, S. J., Lipman, M. D., & Strait,
835 M. M. (2015). Hypervelocity cratering and disruption of porous pumice targets: Implications
836 for crater production, catastrophic disruption, and momentum transfer on porous asteroids.
837 *Planetary and Space Science*, 107, 64 – 76. <https://doi.org/10.1016/j.pss.2014.10.007>
- 838 Garry, W., Robinson, M., Zimbelman, J., Bleacher, J., Hawke, B., Crumpler, L., et al. (2012),
839 The origin of Ina: Evidence for inflated lava flows on the Moon, *Journal of Geophysical*
840 *Research: Planets*, 117, E00H31. <https://doi.org/10.1029/2011JE003981>
- 841 Garry, W. B., Hawke, B. R., Crites, S., Giguere, T., & Lucey, P. G. (2013). Optical maturity
842 (OMAT) of Ina 'D-Caldera', the Moon. *44th Lunar and Planetary Science Conference*, Lunar
843 and Planetary Institute, The Woodlands, Texas, abstract #3058.
- 844 Gault, D. E., Quaide, W. L., & Oberbeck, V. R. (1968). Impact cratering mechanics and
845 structure. In B. M. French & N. M. Short (Eds.), *Shock Metamorphism of Natural Materials*,
846 (pp. 87-100). Baltimore, MD.: Mono Press.
- 847 Head, J., & Gifford, A. (1980). Lunar mare domes: Classification and modes of origin. *The*
848 *Moon and the Planets*. 22, 235-258. <https://doi.org/doi:10.1007/BF00898434>
- 849 Head, J. W., & Ivanov, B. A. (2019). Ina Irregular Mare Patch (IMP): New insights from
850 observations of superposed impact craters, *The 10th Moscow Solar System Symposium*, Space
851 Research Institute, Moscow, Russia, abstract #MS3-PS-32.
- 852 Head, J. W., & Wilson, L. (1992). Lunar mare volcanism: Stratigraphy, eruption conditions, and
853 the evolution of secondary crusts. *Geochimica et Cosmochimica Acta*, 56(6), 2155-2175.
854 [https://doi.org/10.1016/0016-7037\(92\)90183-J](https://doi.org/10.1016/0016-7037(92)90183-J)
- 855 Head, J. W., & Wilson, L. (2017). Generation, ascent and eruption of magma on the Moon: New
856 insights into source depths, magma supply, intrusions and effusive/explosive eruptions (Part 2:

- 857 Predicted emplacement processes and observations). *Icarus*, 283, 176-223.
858 <https://doi.org/10.1016/j.icarus.2016.05.031>
- 859 Head, J. W. & Wilson, L. (2019). Rethinking lunar mare basalt regolith formation: New concepts
860 of lava flow protolith and evolution of regolith thickness and internal structure. *50th Lunar
861 and Planetary Science Conference*, Lunar and Planetary Institute, The Woodlands, Texas,
862 abstract #2532.
- 863 Henriksen, M. R., Manheim, M. R., Burns, K. N., Seymour, P., Speyerer, E. J., Deran, A., et al.
864 (2017). Extracting accurate and precise topography from LROC narrow angle camera stereo
865 observations. *Icarus*, 283, 122-137. <https://doi.org/10.1016/j.icarus.2016.05.012>
- 866 Hiesinger, H., Head, J. W., Wolf, U., Jaumann, R., & Neukum, G. (2011). Ages and stratigraphy
867 of lunar mare basalts: A synthesis. *Geological Society of America Special Papers*, 477, 1-51.
868 [https://doi.org/10.1130/2011.2477\(01\)](https://doi.org/10.1130/2011.2477(01))
- 869 Hörz, F. (1977). Impact cratering and regolith dynamics. *Physics and Chemistry of the Earth*, 10,
870 3-15. [https://doi.org/10.1016/0079-1946\(77\)90003-9](https://doi.org/10.1016/0079-1946(77)90003-9)
- 871 Housen, K. R., Sweet, W. J., & Holsapple, K. A. (2018). Impacts into porous asteroids. *Icarus*,
872 300, 72-96. <https://doi.org/10.1016/j.icarus.2017.08.019>
- 873 Ivanov, B. A., & Head, J. W. (2019). Impacts into magmatic foam and the age of irregular mare
874 patches: Experimental data, interpretations, and outstanding questions, *50th Lunar and
875 Planetary Science Conference*, Lunar and Planetary Institute, The Woodlands, Texas, abstract
876 #1243.
- 877 Langevin, Y., & Arnold, J. R. (1977). The evolution of the lunar regolith. *Annual Review of
878 Earth and Planetary Sciences*, 5(1), 449-489.
879 <https://doi.org/10.1146/annurev.ea.05.050177.002313>
- 880 Lemelin, M., Lucey, P. G., Song, E., & Taylor, G. J. (2015). Lunar central peak mineralogy and
881 iron content using the Kaguya Multiband Imager: Reassessment of the compositional structure
882 of the lunar crust. *Journal of Geophysical Research: Planets*, 120(5), 869-887.
883 <https://doi.org/10.1002/2014je004778>
- 884 Lena, R., Wöhler, C., Phillips, J., Wirths, M., & Bregante, M. T. (2007). Lunar domes in the
885 Doppelmayr region: Spectrophotometry, morphometry, rheology, and eruption conditions.
886 *Planetary and Space Science*, 55(10), 1201-1217. <https://doi.org/10.1016/j.pss.2007.01.007>
- 887 Lena, R., Wöhler, C., Bregante, M. T., Lazzarotti, P., & Lammel, S. (2008). Lunar domes in
888 Mare Undarum: Spectral and morphometric properties, eruption conditions, and mode of
889 emplacement. *Planetary and Space Science*, 56(3), 553-569.
890 <https://doi.org/10.1016/j.pss.2007.11.010>
- 891 Liu, J., Li, C., Wang, W., Zeng, X., Mu, L., & Yang, Y. (2019). Extraction of lunar domes from
892 Chang'E-2 data with new method. *Icarus*, 321, 29-33.
893 <https://doi.org/10.1016/j.icarus.2018.10.030>
- 894 Lucey, P., Korotev, R. L., Gillis, J. J., Taylor, L. A., Lawrence, D., Campbell, B. A., et al.
895 (2006). Understanding the lunar surface and space-Moon interactions. *Reviews in Mineralogy
896 & Geochemistry*, 60, 83-219. <https://doi.org/10.2138/rmg.2006.60.2>
- 897 Kadono, T. (1999). Hypervelocity impact into low density material and cometary outburst.
898 *Planetary and Space Science*, 47(3), 305-318. [https://doi.org/10.1016/S0032-0633\(98\)00039-7](https://doi.org/10.1016/S0032-0633(98)00039-7)
- 899 McKay, D. S., Heiken, G., Basu, A., Blanford, G., Simon, S., Reedy, R., et al. (1991). The lunar
900 regolith. In G. H. Heiken, D. T. Vaniman, & B. M. French (Eds.), *Lunar sourcebook* (pp. 285
901 - 356). Cambridge: Cambridge University Press.

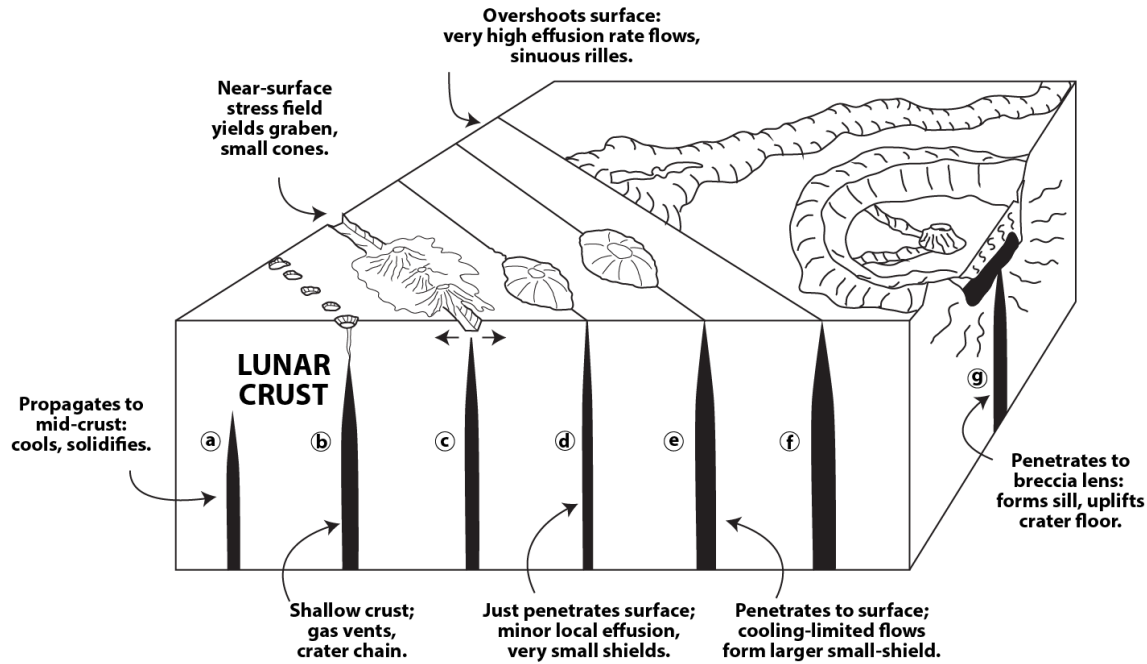
- 902 Michael, G. G. & Neukum, G. (2010). Planetary surface dating from crater size-frequency
903 distribution measurements: Partial resurfacing events and statistical age uncertainty. *Earth and*
904 *Planetary Science Letters*, 294(3-4), 223-229. <https://doi.org/10.1016/j.epsl.2009.12.041>
- 905 Michael, G. G., Kneissl, T., & Neesemann, A. (2016). Planetary surface dating from crater size-
906 frequency distribution measurements: Poisson timing analysis. *Icarus*, 277, 279-285.
907 <https://dx.doi.org/10.1016/j.icarus.2016.05.019>
- 908 Neish, C. D., Hamilton, C. W., Hughes, S. S., Nawotniak, S. K., Garry, W. B., Skok, J. R., et al.
909 (2017). Terrestrial analogues for lunar impact melt flows. *Icarus*, 281, 73-89.
910 <https://doi.org/10.1016/j.icarus.2016.08.008>
- 911 Neukum, G., Ivanov, B. A., & Hartmann, W. K. (2001). Cratering records in the inner solar
912 system in relation to the lunar reference system. *Space Science Reviews*, 96(1-4), 55-86.
- 913 Ohtake, M., Haruyama, J., Matsunaga, T., Yokota, Y., Morota, T., Honda, C., & LISM team
914 (2008). Performance and scientific objectives of the SELENE (KAGUYA) Multiband Imager,
915 *Earth Planets Space*, 60, 257-264. <https://doi.org/10.1186/BF03352789>
- 916 Okamoto, T., & Nakamura, A. M. (2017). Scaling of impact-generated cavity-size for highly
917 porous targets and its application to cometary surfaces. *Icarus*, 292, 234-244.
918 <https://doi.org/10.1016/j.icarus.2017.01.007>
- 919 Parfitt, E. A., & Wilson, L. (1995). Explosive volcanic eruptions—IX. The transition between
920 Hawaiian-style lava fountaining and Strombolian explosive activity. *Geophysical Journal*
921 *International*, 121(1), 226-232. <https://doi.org/10.1111/j.1365-246X.1995.tb03523.x>
- 922 Peck, D. L., Wright, T. L., & Decker, R. W. (1979). The lava lakes of Kilauea. *Scientific American*,
923 241(4), 114-129. <https://www.scientificamerican.com/article/the-lava-lakes-of-kilauea/>
- 924 Qiao, L., Xiao, Z., Zhao, J., & Xiao, L. (2016). Subsurface structures at the Chang'e-3 landing
925 site: Interpretations from orbital and in-situ imagery data. *Journal of Earth Science*, 27(4),
926 707-715. <http://dx.doi.org/10.1007/s12583-015-0655-3>
- 927 Qiao, L., Head, J., Wilson, L., Xiao, L., Kreslavsky, M., & Dufek, J. (2017). Ina pit crater on the
928 Moon: Extrusion of waning-stage lava lake magmatic foam results in extremely young crater
929 retention ages. *Geology*, 45(5), 455-458. <https://doi.org/10.1130/G38594.1>
- 930 Qiao, L., Head, J. W., Xiao, L., Wilson, L., & Dufek, J. D. (2018). The role of substrate
931 characteristics in producing anomalously young crater retention ages in volcanic deposits on
932 the Moon: Morphology, topography, sub-resolution roughness and mode of emplacement of
933 the Sosigenes Lunar Irregular Mare Patch (IMP). *Meteoritics & Planetary Science*, 53(4), 778-
934 812. <https://doi.org/10.1111/maps.13003>
- 935 Qiao, L., Head, J. W., Ling, Z., Wilson, L., Xiao, L., Dufek, J. D., & Yan, J. (2019a). Geological
936 characterization of the Ina shield volcano summit pit crater on the Moon: Evidence for
937 extrusion of waning-stage lava lake magmatic foams and anomalously young crater retention
938 ages. *Journal of Geophysical Research: Planets*, 124(4), 1100-1140.
939 <https://doi.org/10.1029/2018JE005841>
- 940 Qiao, L., Head, J. W., Ling, Z., & Wilson, L. (2019b). Exploring a sub-classification scheme for
941 Irregular Mare Patches (IMPs), *50th Lunar and Planetary Science Conference*, Lunar and
942 Planetary Institute, The Woodlands, Texas, abstract #2358.
- 943 Quaide, W. L., & Oberbeck, V. R. (1968). Thickness determinations of the lunar surface layer
944 from lunar impact craters. *Journal of Geophysical Research*, 73(16), 5247-5270.
945 <http://dx.doi.org/10.1029/JB073i016p05247>
- 946 Ripepe, M., Donne, D. D., Harris, A., Marchetti, E., & Ulivieri, G. (2008). Dynamics of
947 strombolian activity, In S. Calvari, S. Inguaggiato, G. Puglisi, M. Ripepe, & M. Rosi (Eds.),

- 948 *The stromboli volcano: An integrated study of the 2002–2003 eruption*, AGU Geophysical
949 Monograph Series (Vol. 182, pp. 39–48). Washington, DC: American Geophysical Union.
950 <https://doi.org/10.1029/182GM05>
- 951 Robinson, M. S., Brylow, S. M., Tschimmel, M., Humm, D., Lawrence, S. J., Thomas, P. C., et
952 al. (2010). Lunar Reconnaissance Orbiter Camera (LROC) instrument overview. *Space*
953 *Science Reviews*, 150(1), 81-124. <https://doi.org/10.1007/s11214-010-9634-2>
- 954 Robinson, M. S., Ashley, J. W., Boyd, A. K., Wagner, R. V., Speyerer, E. J., Ray Hawke, B., et
955 al. (2012). Confirmation of sublunarean voids and thin layering in mare deposits. *Planetary*
956 *and Space Science*, 69(1), 18-27. <https://doi.org/10.1016/j.pss.2012.05.008>
- 957 Rutherford, M. J., Head, J. W., Saal, A. E., Hauri, E., & Wilson, L. (2017). Model for the origin,
958 ascent, and eruption of lunar picritic magmas. *American Mineralogist*, 102(10), 2045-2053.
959 <https://dx.doi.org/10.2138/am-2017-5994ccbyncnd>
- 960 Schultz, P. H., Staid, M. I., & Pieters, C. M. (2006). Lunar activity from recent gas release.
961 *Nature*, 444(7116), 184-186. <https://doi.org/10.1038/nature05303>
- 962 Staid, M. I., & Pieters, C. M. (2000). Integrated spectral analysis of mare soils and craters:
963 Applications to eastern nearside basalts. *Icarus*, 145(1), 122-139.
964 <https://doi.org/10.1006/icar.1999.6319>
- 965 Staid, M., Isaacson, P., Petro, N., Boardman, J., Pieters, C. M., Head, J. W., et al. (2011). The
966 spectral properties of Ina: New observations from the Moon Mineralogy Mapper. *42nd Lunar*
967 *and Planetary Science Conference*, Lunar and Planetary Institute, The Woodlands, Texas,
968 abstract #2499.
- 969 Stooke, P. J. (2012). Lunar meniscus hollows. *43rd Lunar and Planetary Science Conference*,
970 Lunar and Planetary Institute, The Woodlands, Texas, abstract #1011.
- 971 Stopar, J. D., Robinson, M. S., van der Bogert, C. H., Hiesinger, H., Ostrach, L. R., Giguere, T.
972 A., & Lawrence, S. J. (2017). Young lunar volcanism: Irregular mare patches as drained lava
973 ponds and inflated flows. *48th Lunar and Planetary Science Conference*, Lunar and Planetary
974 Institute, The Woodlands, Texas, abstract #1792.
- 975 Strain, P. L., & El-Baz, F. (1980). The geology and morphology of Ina. In *Proceedings of the*
976 *11th Lunar Science Conference* (pp. 2437-2446).
- 977 Taylor, S. R. (1989). Growth of planetary crusts. *Tectonophysics*, 161(3), 147-156.
978 [https://doi.org/10.1016/0040-1951\(89\)90151-0](https://doi.org/10.1016/0040-1951(89)90151-0)
- 979 Tilling, R. I. (1987). Fluctuations in surface height of active lava lakes during 1972–1974 Mauna
980 Ulu Eruption, Kilauea Volcano, Hawaii. *Journal of Geophysical Research: Solid Earth*,
981 92(B13), 13721-13730. <https://doi.org/10.1029/JB092iB13p13721>
- 982 Tilling, R. I., Christiansen, R. I., Duffield, W. A., Endo, E. T., Holcomb, R. T., Koyanagi, R. Y. ,
983 Peterson, D. W., & Unger, J. D. (1987). The 1972–1974 Mauna Ulu eruption, Kilauea volcano: An
984 example of quasi-steady-state magma transfer, In R. W. Decker, T. L. Wright, & P. H. Stauffer (Eds.),
985 *Volcanism in Hawaii*, U.S. Geological Survey Professional Paper 1350 (pp. 405–469). Washington:
986 United States Government Printing Office.
- 987 Trask, N. J. (1966). Size and spatial distribution of craters estimated from the Ranger
988 photographs, In *Ranger VIII and IX, Part II, Experimenters' Analyses and Interpretations*
989 (JPL Technical Reports 32-800, pp. 252-264). Pasadena, CA: Jet Propulsion Lab.
- 990 Tye, A. R., & Head, J. W. (2013). Mare Tranquillitatis: Distribution of mare domes, relation to
991 broad mare rise, and evidence of a previously unrecognized basin from LOLA altimetric data.
992 *44th Lunar and Planetary Science Conference*, Lunar and Planetary Institute, The Woodlands,
993 Texas, abstract #1319.

- 994 Valantinas, A., Kinch, K. M., & Bridžius, A. (2018). Low crater frequencies and low model ages
995 in lunar maria: Recent endogenic activity or degradation effects? *Meteoritics & Planetary*
996 *Science*, 53(4), 826-838. <https://doi.org/10.1111/maps.13033>
- 997 Whitaker, E. A. (1972). An unusual mare feature, In *Apollo 15 Preliminary Science Report*
998 (NASA SP-289, pp. 25-84–25-85).
- 999 Wilcox, B. B., Robinson, M. S., Thomas, P. C., & Hawke, B. R. (2005). Constraints on the depth
1000 and variability of the lunar regolith. *Meteoritics & Planetary Science*, 40(5), 695-710.
1001 <https://doi.org/10.1111/j.1945-5100.2005.tb00974.x>
- 1002 Wieczorek, M. A., Jolliff, B. L., Khan, A., Pritchard, M. E., Weiss, B. P., Williams, J. G., et al.
1003 (2006). The constitution and structure of the lunar interior. *Reviews in Mineralogy and*
1004 *Geochemistry*, 60(1), 221-364. <https://doi.org/10.2138/rmg.2006.60.3>
- 1005 Wilson, L., & Head, J. W. (1981). Ascent and eruption of basaltic magma on the Earth and
1006 Moon. *Journal of Geophysical Research: Solid Earth*, 86(B4), 2971-3001.
1007 <https://doi.org/10.1029/JB086iB04p02971>
- 1008 Wilson, L., & Head, J. W. (2003). Deep generation of magmatic gas on the Moon and
1009 implications for pyroclastic eruptions. *Geophysical Research Letters*, 30(12).
1010 <https://doi.org/10.1029/2002GL016082>
- 1011 Wilson, L., & Head, J. W. (2017a). Eruption of magmatic foams on the Moon: Formation in the
1012 waning stages of dike emplacement events as an explanation of “irregular mare patches”.
1013 *Journal of Volcanology and Geothermal Research*, 335, 113-127,
1014 <https://doi.org/10.1016/j.jvolgeores.2017.02.009>.
- 1015 Wilson, L., & Head, J. W. (2017b). Generation, ascent and eruption of magma on the Moon:
1016 New insights into source depths, magma supply, intrusions and effusive/explosive eruptions
1017 (Part 1: Theory). *Icarus*, 283, 146-175, <https://doi.org/10.1016/j.icarus.2015.12.039>.
- 1018 Wilson, L., & Head, J. W. (2018). Controls on lunar basaltic volcanic eruption structure and
1019 morphology: Gas release patterns in sequential eruption phases. *Geophysical Research Letters*,
1020 45, 5852–5859. <https://doi.org/10.1029/2018GL078327>
- 1021 Wilson, L., Head, J. W., & Zhang, F. (2019). A theoretical model for the formation of Ring Moat
1022 Dome Structures: Products of second boiling in lunar basaltic lava flows. *Journal of*
1023 *Volcanology and Geothermal Research*, 374, 160-180.
1024 <https://doi.org/10.1016/j.jvolgeores.2019.02.018>
- 1025 Wöhler, C., Lena, R., Lazzarotti, P., Phillips, J., Wirths, M., & Pujic, Z. (2006). A combined
1026 spectrophotometric and morphometric study of the lunar mare dome fields near Cauchy, Arago,
1027 Hortensius, and Milichius. *Icarus*, 183(2), 237-264. <https://doi.org/10.1016/j.icarus.2006.03.003>
- 1028 Wöhler, C., Lena, R., & Phillips, J. (2007). Formation of lunar mare domes along crustal fractures:
1029 Rheologic conditions, dimensions of feeder dikes, and the role of magma evolution. *Icarus*, 189(2),
1030 279-307. <https://doi.org/10.1016/j.icarus.2007.01.011>
- 1031 Wolfe, E. W., Garcia, M. O., Jackson, D. B., Koyanagi, R. Y., Neal, C. A., & Okamura, A. T. (1987),
1032 The Puu Oo eruption of Kilauea Volcano, Episodes 1–20, January 3, 1983, to June 8, 1984, In R. W.
1033 Decker, T. L. Wright, & P. H. Stauffer (Eds.), *Volcanism in Hawaii*, U.S. Geological Survey
1034 Professional Paper 1350 (pp. 471–508). Washington: United States Government Printing Office.
- 1035 Yasui, M., Matsumoto, E., & Arakawa, M. (2015). Experimental study on impact-induced seismic wave
1036 propagation through granular materials. *Icarus*, 260, 320-331.
1037 <https://doi.org/10.1016/j.icarus.2015.07.032>
- 1038 Zhang, F., Zhu, M. H., Bugiolacchi, R., Huang, Q., Osinski, G. R., Xiao, L., & Zou, Y. L.
1039 (2018). Diversity of basaltic lunar volcanism associated with buried impact structures:

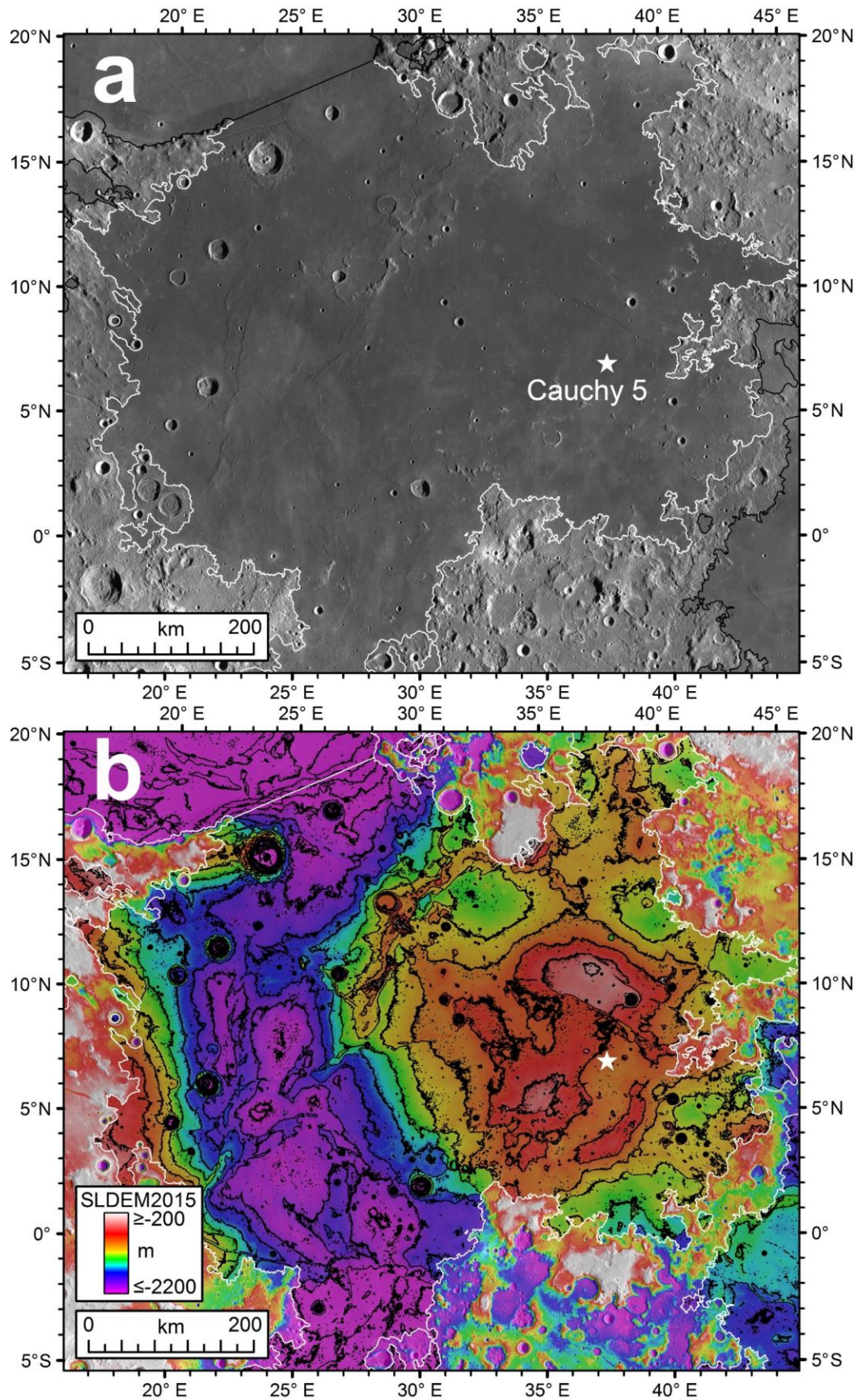
1040 Implications for intrusive and extrusive events. *Icarus*, 307, 216-234.
1041 <https://doi.org/10.1016/j.icarus.2017.10.039>

1042 **Figures:**

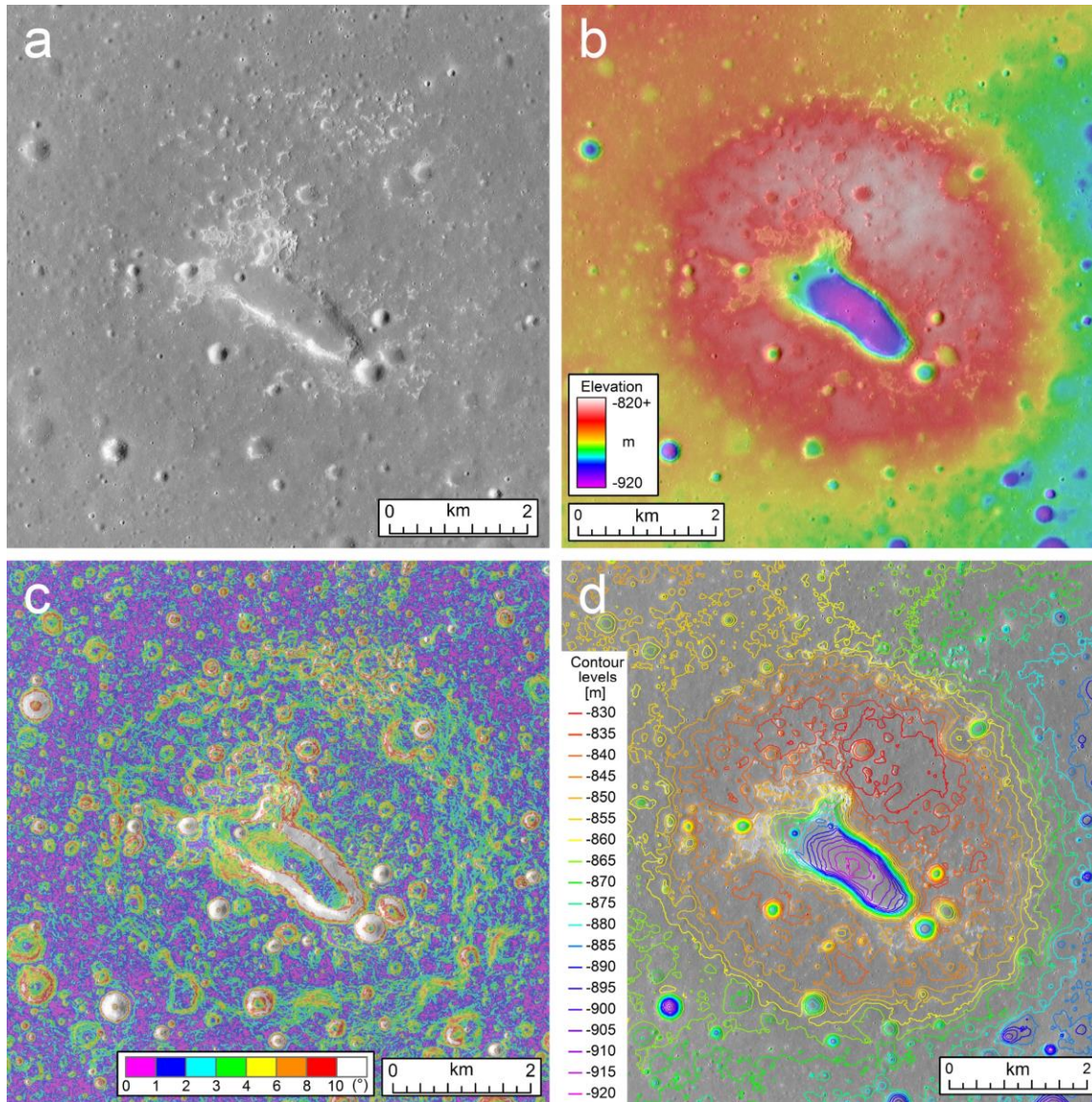


1043

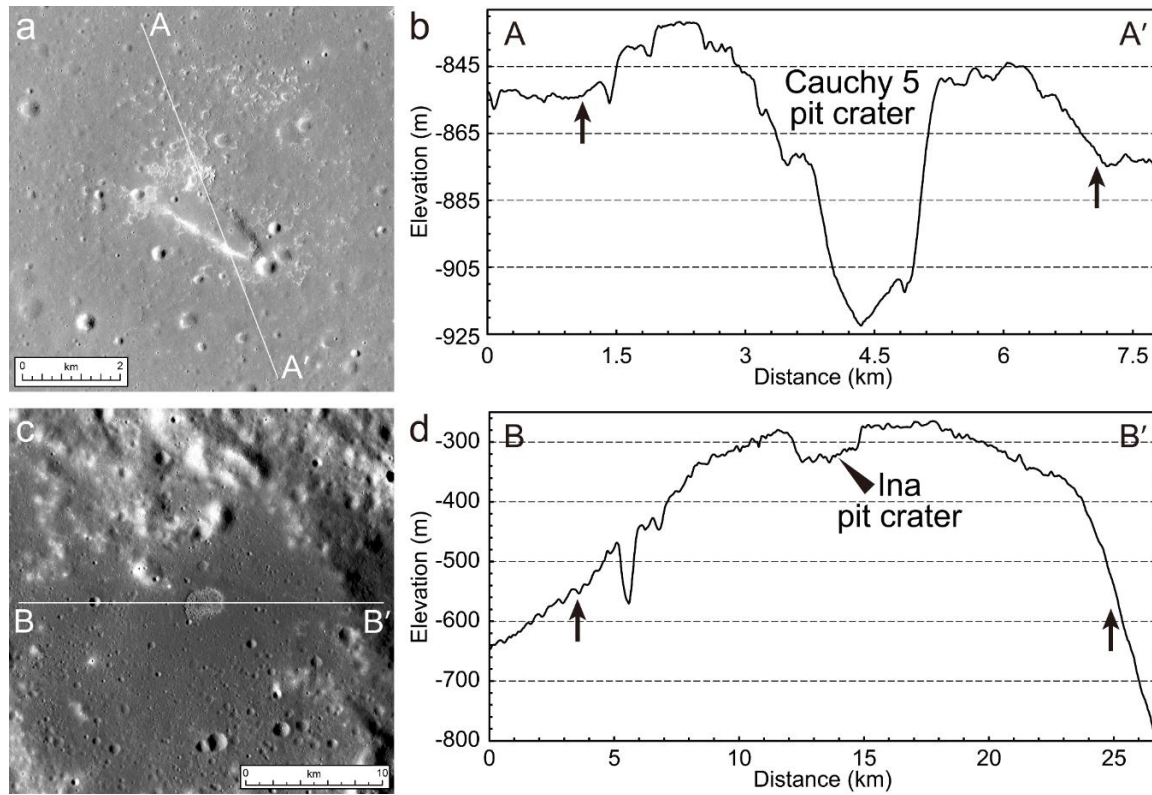
1044 **Figure 1.** Synthesis block diagram of mare basalt dikes approaching, intruding, stalling and
 1045 erupting on the Moon. Small shield volcanoes (d, e) represent relatively small-volume, low
 1046 magma rise rate eruptions compared with much larger dikes (f) that form high-volume, high
 1047 effusion rate eruptions. The Cauchy 5 small shield (5-6 km diameter) lies at the small end of the
 1048 eruption volume (d) compared to the larger (e), ~25 km diameter, Ina small shield volcano
 1049 (Figure 4).



1051 **Figure 2.** Geologic setting of the Cauchy 5 small shield volcano in Mare Tranquillitatis: (a)
 1052 LROC WAC (Robinson et al., 2010) low-sun mosaic, the boundary of Mare Tranquillitatis are
 1053 delineated by white outlines, other maria by black outlines and the location of Cauchy 5 small
 1054 shield is indicated by the white star, (b) SLDEM2015 (SELENE-TC+LRO-LOLA merged DEM,
 1055 Barker et al., 2016) topography, with 200 m-interval contour overlain (only for mare regions
 1056 outlined by white polygons). The projection is lambert conformal conic projection, with central
 1057 meridian of 30°E and standard parallels of 2°N and 16°N, and north is up.

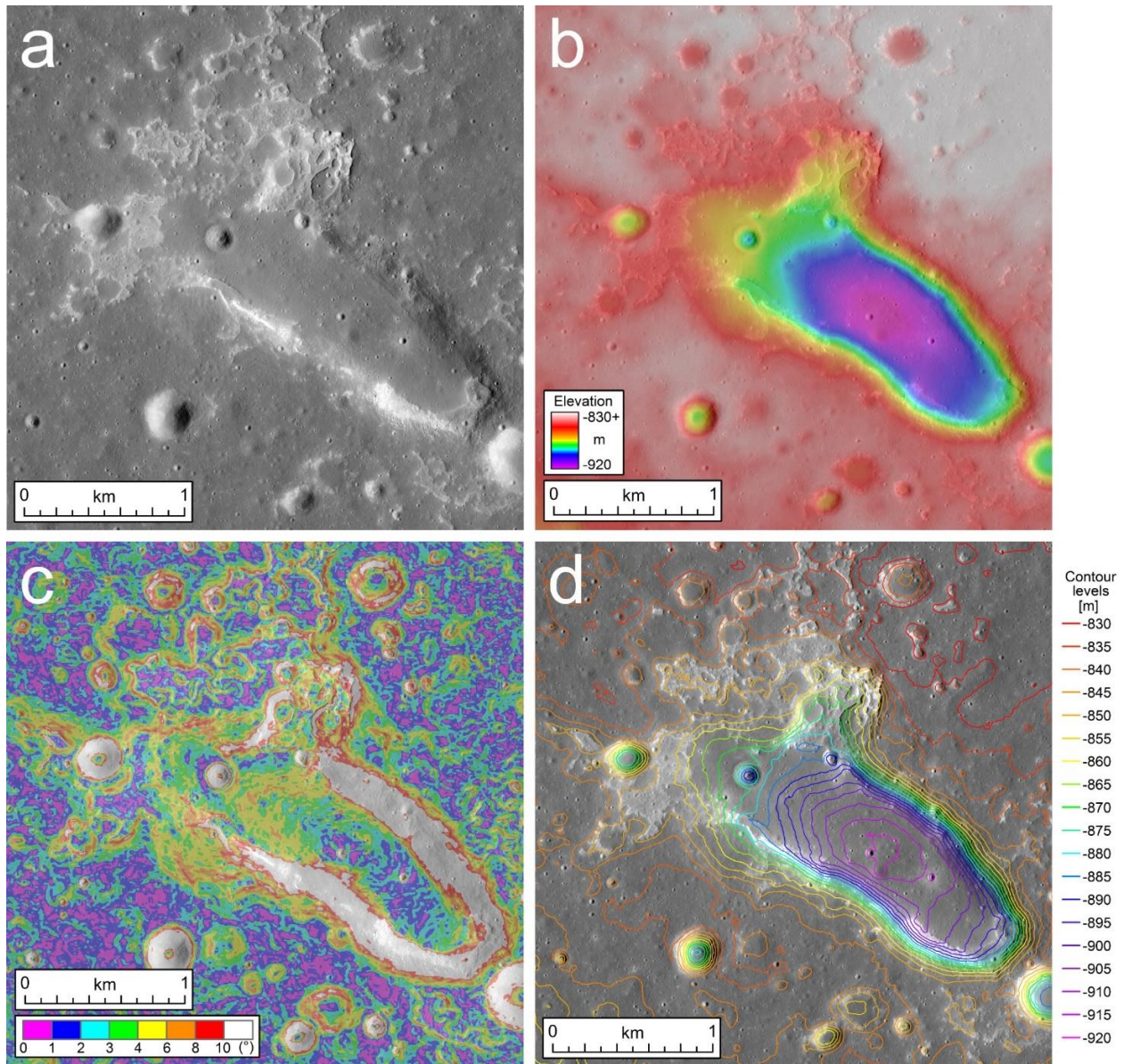


1058
 1059 **Figure 3.** Cauchy 5 small shield volcano mapped by LROC NAC: (a) LROC NAC image (frame
 1060 M1108025067, 1.2 m/pixel), (b) LROC NAC DTM topography (5 m/pixel; Robinson et al., 2010;
 1061 Henriksen et al., 2017), (c) NAC DTM-derived slope map (15 m baseline) and (d) 5 m contour
 1062 interval map. All the images of the Cauchy 5 feature in this work are in a sinusoidal projection
 1063 centered at 37.592°E, and north is up.



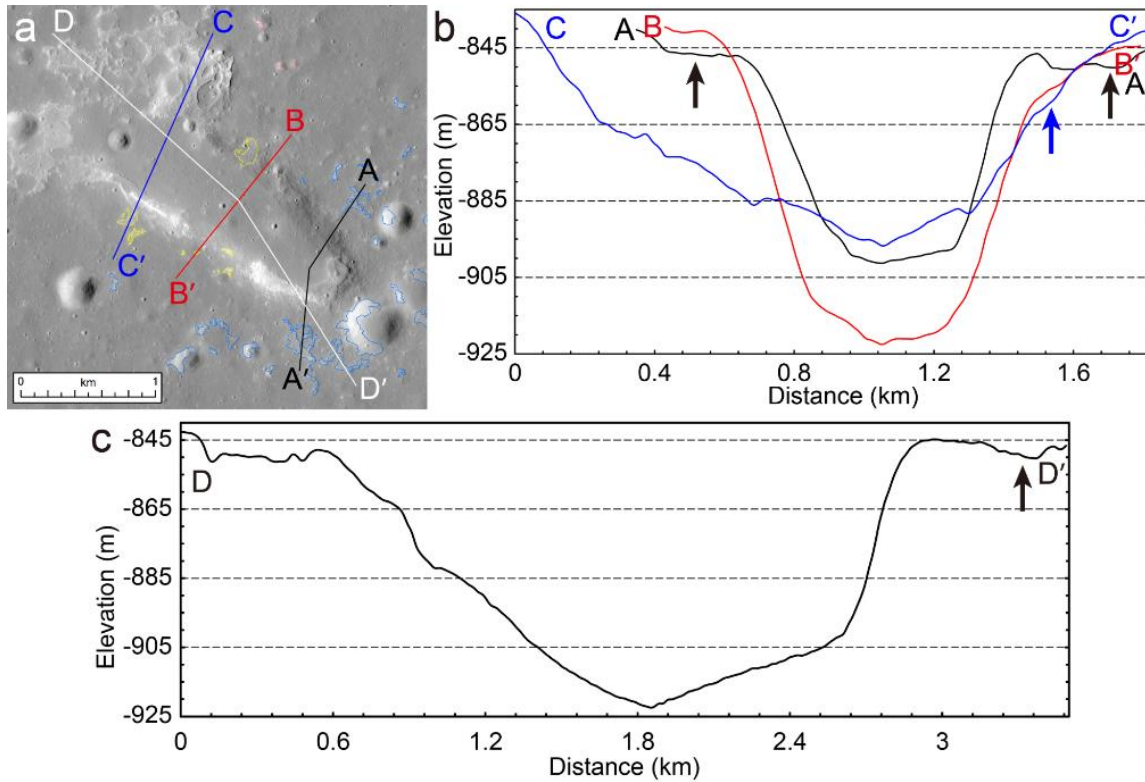
1064

1065 **Figure 4.** LROC NAC DTM topographic profiles (5 m spatial sampling size) across the Cauchy
 1066 5 small shield volcano (panels a, b) and its comparison with the much larger Ina shield volcano
 1067 (2 m spatial sampling size; panels c, d). The arrows in panels (b) and (d) mark the location of the
 1068 base of the shields, and the locations of the Cauchy and Ina summit pit craters are labeled. Panel
 1069 (c) is a sinusoidal projection centered at 5.3473°E, and north is up.



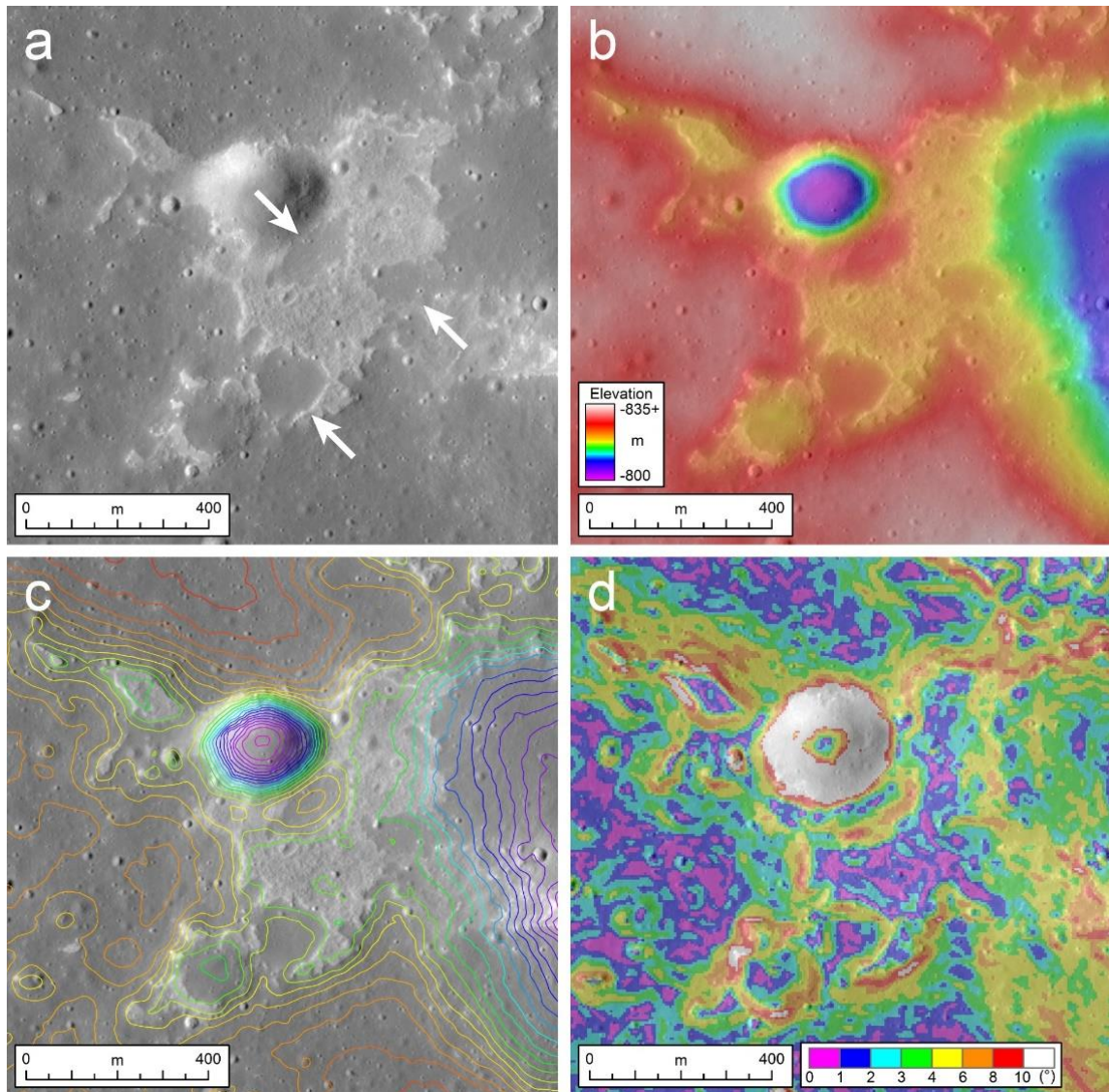
1070

1071 **Figure 5.** Cauchy 5 small shield volcano summit pit crater: (a) LROC NAC frame
 1072 M1108025067, 1.2 m/pixel, (b) LROC NAC DTM topography overlain on NAC M1108025067,
 1073 (c) NAC DTM-derived slope map and (d) 5 m contour interval overlaid on NAC image.



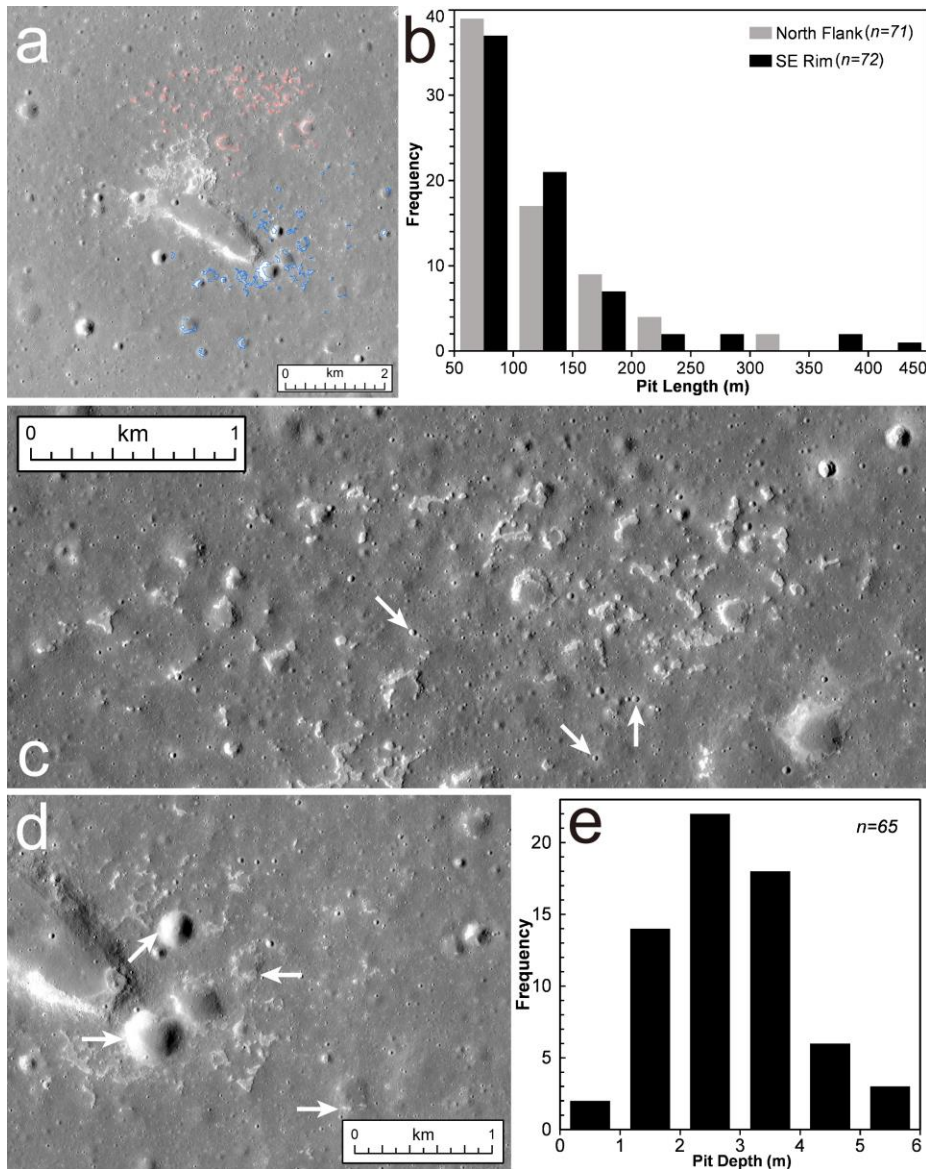
1074

1075 **Figure 6.** LROC NAC DTM topographic profiles (b) across and (c) along the Cauchy 5 eruptive
 1076 vent; the locations of these profiles are shown in panel (a), LROC NAC image M1108025067.
 1077 Color polygons in panel (a) are mapped small mare IMP-like pits in different locations: pink:
 1078 northern flank; blue: southeastern rim; yellow: other regions (see Figure 8a for the complete
 1079 mapping result). Arrows in the topographic profiles show the location of small IMP-like pits:
 1080 black arrows for pits on the path of profile AA' and blue arrows for pits on the path of profile
 1081 CC'.



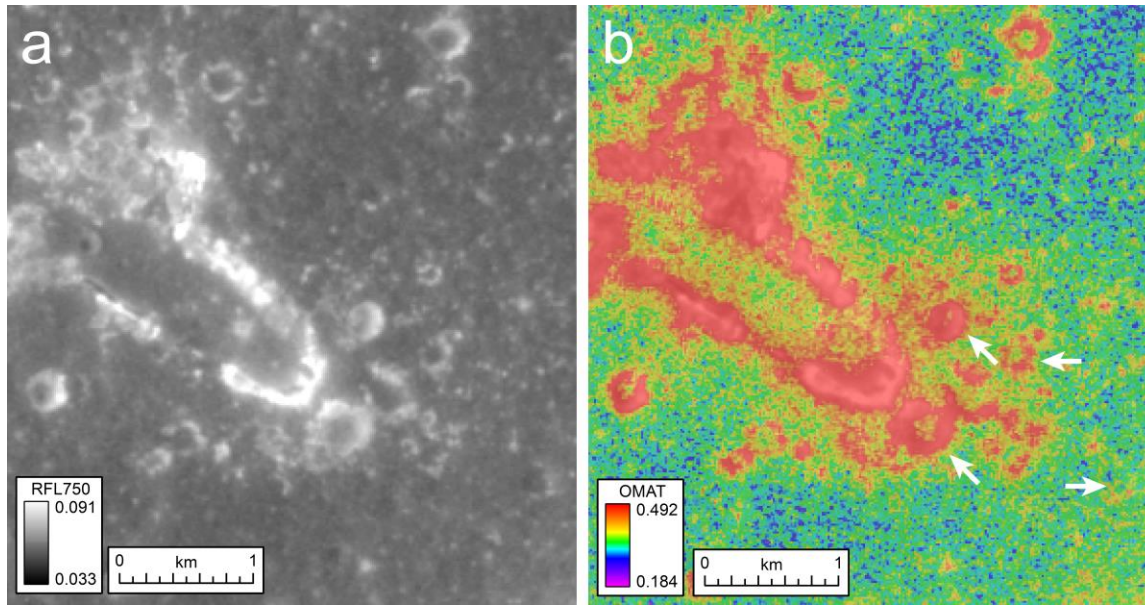
1082

1083 **Figure 7.** Image and topographic maps of the NW rim of Cauchy 5 shield volcano. (a) LROC
 1084 NAC image M1108025067, (b) NAC DTM topography, (c) 2 m contour interval (magenta and
 1085 purple contours for lower elevations and red and yellow for higher elevations) and (d) NAC
 1086 DTM slope overlaid on LROC NAC image. The white arrows in panel (a) indicate the mound
 1087 terrains occurring on the NW rim, which is surrounded by bright and rough terrains.



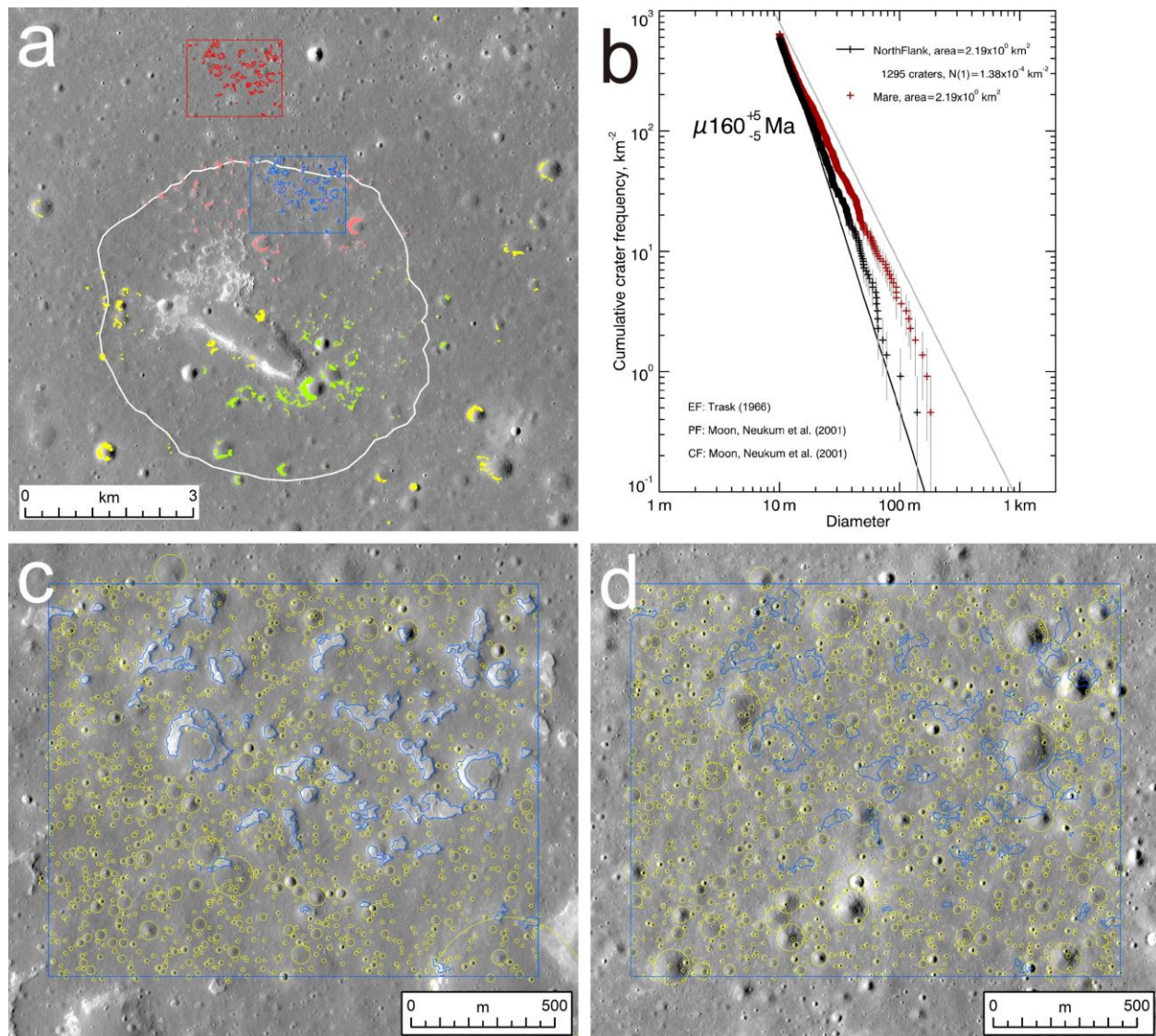
1088

1089 **Figure 8.** Volcano flank pit craters: (a) Spatial distribution (base map is a portion of LROC NAC
 1090 M1108025067), (b) length-frequency distributions of the abundant small pit-type IMPs ≥ 50 m in
 1091 length mapped in the north shield flank (pink polygons) and southeast rim (blue polygons) and
 1092 (e) depth-frequency distribution of all pits ≥ 50 m in length on relatively flat surfaces ($n = 65$). (c)
 1093 Detailed image of the northern shield flank pit-type IMP occurrences, LROC NAC frame
 1094 M1108025067. The white arrows indicate examples of post-foam overflow impact craters,
 1095 interpreted to have penetrated the surface of the foamy flow layer and exposed the underlying
 1096 shield/mare basaltic deposits, generating blocky crater interiors. (d) LROC NAC image
 1097 (M1108025067) of the southeast crater rim pit-type IMP occurrences. The white arrows mark
 1098 several relatively extensive IMP-like pits on the interior walls of some depressions (also noted in
 1099 Figure 9).



1100

1101 **Figure 9.** Kaguya MI (a) 750 nm reflectance (RFL750) and (b) optical maturity (OMAT) maps
 1102 (Ohtake et al., 2008; Lemelin et al., 2015) of the Cauchy 5 pit crater and southeastern rim. The
 1103 arrows in panel (b) mark the relatively extensive mapped pits in Figure 8a and pointed out in
 1104 Figure 8d.



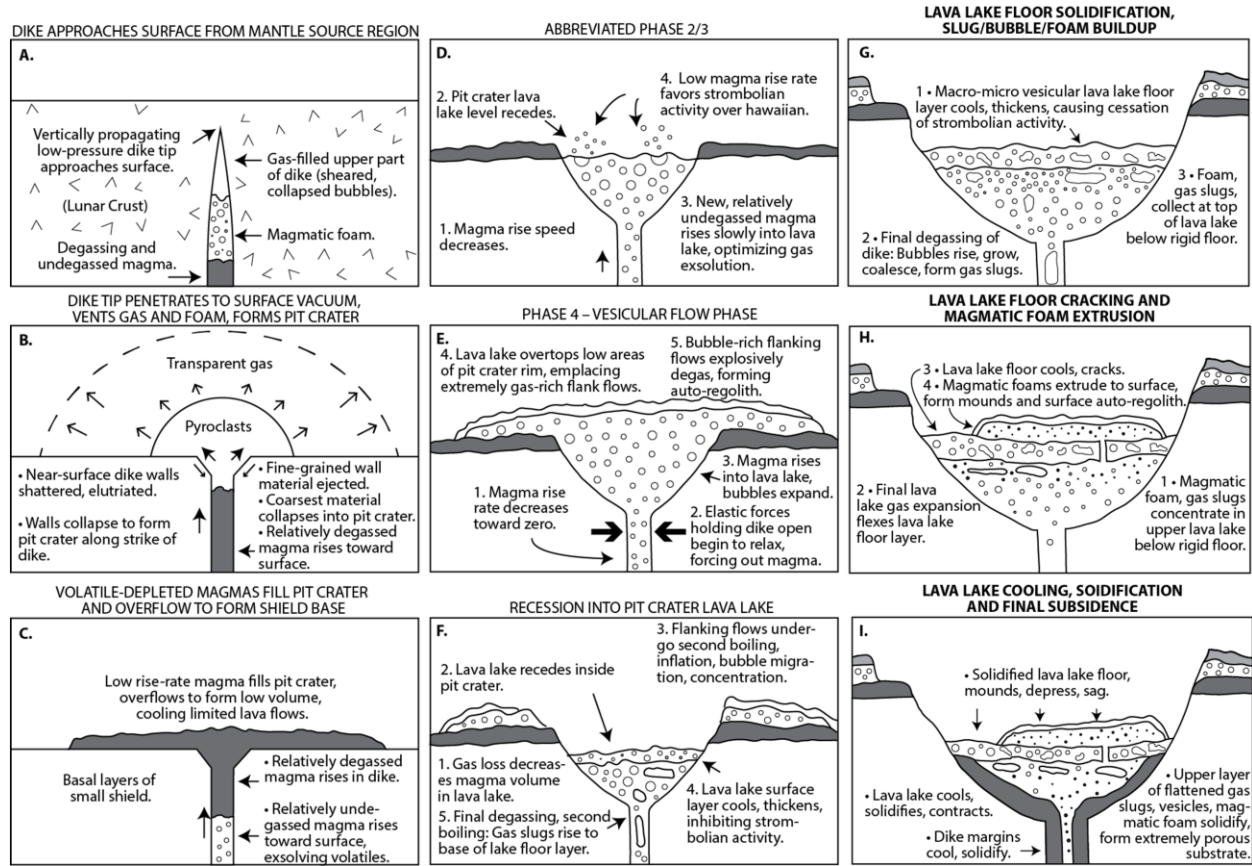
1105

1106 **Figure 10.** (a) Locations of the Cauchy 5 crater population analysis working areas. Blue
 1107 polygons: crater counting area on the shield flank outflows (pitted areas mapped in Figure 8a are
 1108 not included), red polygons: crater counting area on the surrounding mare, with same shape as
 1109 the shield flank flow counting area. The white line is the approximate location of the base of the
 1110 shield. Pink patches are the mapped IMP-like pits on the north flank, green patches are pits on
 1111 the southeast rim and yellow patches are small pits elsewhere. (b) Cumulative size-frequency
 1112 distribution plots of impact craters (diameter ≥ 10 m) superposed on the north shield flank inter-
 1113 pit surface (black crosses) and surrounding mare (red crosses). The gray line on the right is the
 1114 lunar equilibrium function (EF) curve from Trask (1966). Model ages are fitted on the basis of
 1115 the production function (PF) and chronology function (CF) proposed by Neukum et al. (2001),
 1116 using the CraterStats software package (Micheal & Neukum, 2010; Michael et al. 2016): on the
 1117 north shield flank, fitting craters ≥ 10 m in diameter gives a model age of 160 Ma; the crater
 1118 diameter fit ranges are indicated by the horizontal extent of the fitted isochrons; the μ before the
 1119 calculated model ages is the function representing the uncertainty of calibration of the
 1120 chronology model (Michael et al. 2016). (c) Crater count map of the north shield flank inter-pit

1121 surface. (d) Spatial distribution of the counted impact craters on the surrounding mare.
 1122 Background images of panels a, c and d are all cropped from LROC NAC frame 1138873574.

A	PHASE 1	PHASE 2	PHASE 3	PHASE 4	B	PHASE 1	PHASE 2	PHASE 3	PHASE 4
	Eruption Phase	Dike penetrates to surface, transient gas release phase	Dike base still rising, high flux hawaiian eruptive phase	Dike equilibration, lower flux hawaiian to strombolian transition phase		Dike closing, strombolian vesicular flow phase	Eruption Phase	Dike penetrates to surface, transient gas release phase	Dike base decelerates, low flux hawaiian eruptive phase
Dike Configuration					Dike Configuration				
Surface Eruption Style					Surface Eruption Style				
Magma Rise Speed	30 to 20 m/s	20 to 10 m/s	5 to <1 m/s	< 1 m/s	Magma Rise Speed	~ 10 m/s	~ 1 m/s	~ 0.1 m/s	< 0.1 m/s
Magma Volume Flux	~10 ⁶ m ³ /s	10 ⁶ to 10 ⁵ m ³ /s	10 ⁵ to ~10 ⁴ m ³ /s	~10 ⁴ m ³ /s	Magma Volume Flux	~10 ⁴ m ³ /s	~10 ³ m ³ /s	~300 m ³ /s	~100 m ³ /s
Percent Dike Volume Erupted	<5%	~30%	~30%	~35%	Percent Dike Volume Erupted	~ 0.1%	~0.05%	~ 0.1%	~ 0.25%
Phase Duration	~3 minutes	5-10 days	2-3 days	10-100 days	Phase Duration	~3 minutes	~1 hour	~3 days	~10 days
Flow Advance Rate	n/a	~3 to 0.1 m/s	0.03 m/s	0.01 m/s	Flow Advance Rate	n/a	~0.03 m/s	~0.01 m/s	~0.003 m/s
Flow Advance Distance	n/a	300 km	305 km	335 km	Flow Advance Distance	n/a	~100 m	~1 km	~ 2.5 km
Vesicularity of Flow	n/a	zero	low, but increasing	very high	Vesicularity of Flow	n/a	zero	high	very high

1123
 1124 **Figure 11.** The detailed nature of typical phases in mare basalt lava flow eruptions. a) The
 1125 characteristics of the four eruption phases during a typical large-volume, high-effusion rate lunar
 1126 lava flow eruption (Figure 1f), with diagrams and parameters representing average values (from
 1127 Wilson and Head, 2018). The relative duration of individual phases depends on the total dike
 1128 volume and vertical extent. b) In a low-volume, low effusion rate eruption typical of very small
 1129 shield volcanoes such as Cauchy 5 (Figure 1d), Phases 2 and 3 are highly abbreviated, and Phase
 1130 4 is relatively more significant.



1131

1132

1133

1134

1135

1136

1137

1138

1139

1140

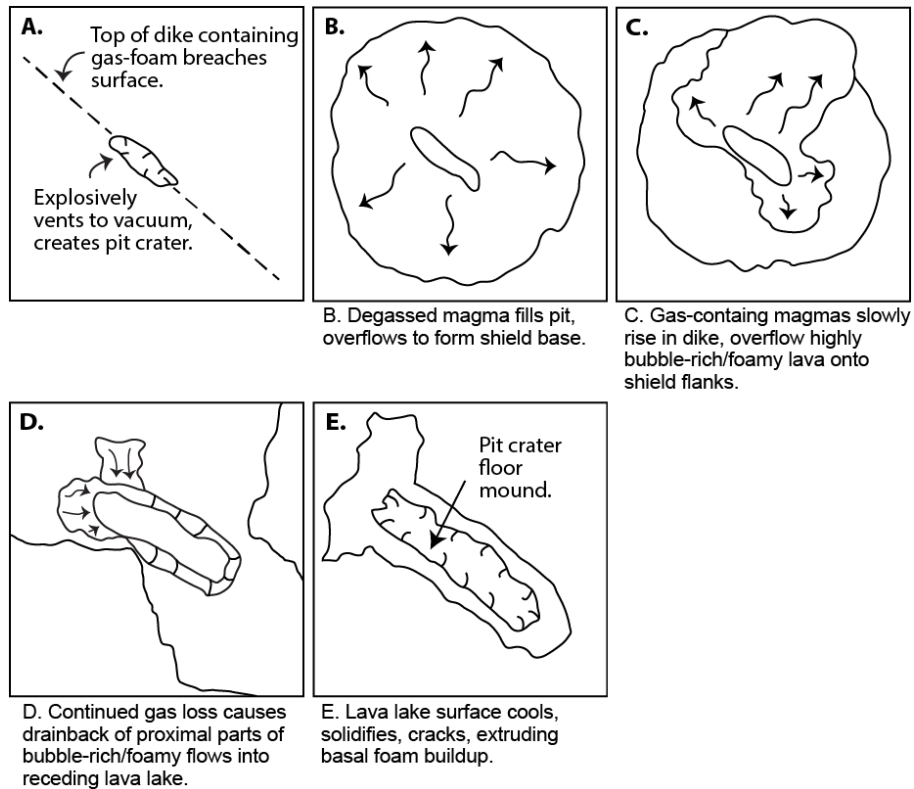
1141

1142

1143

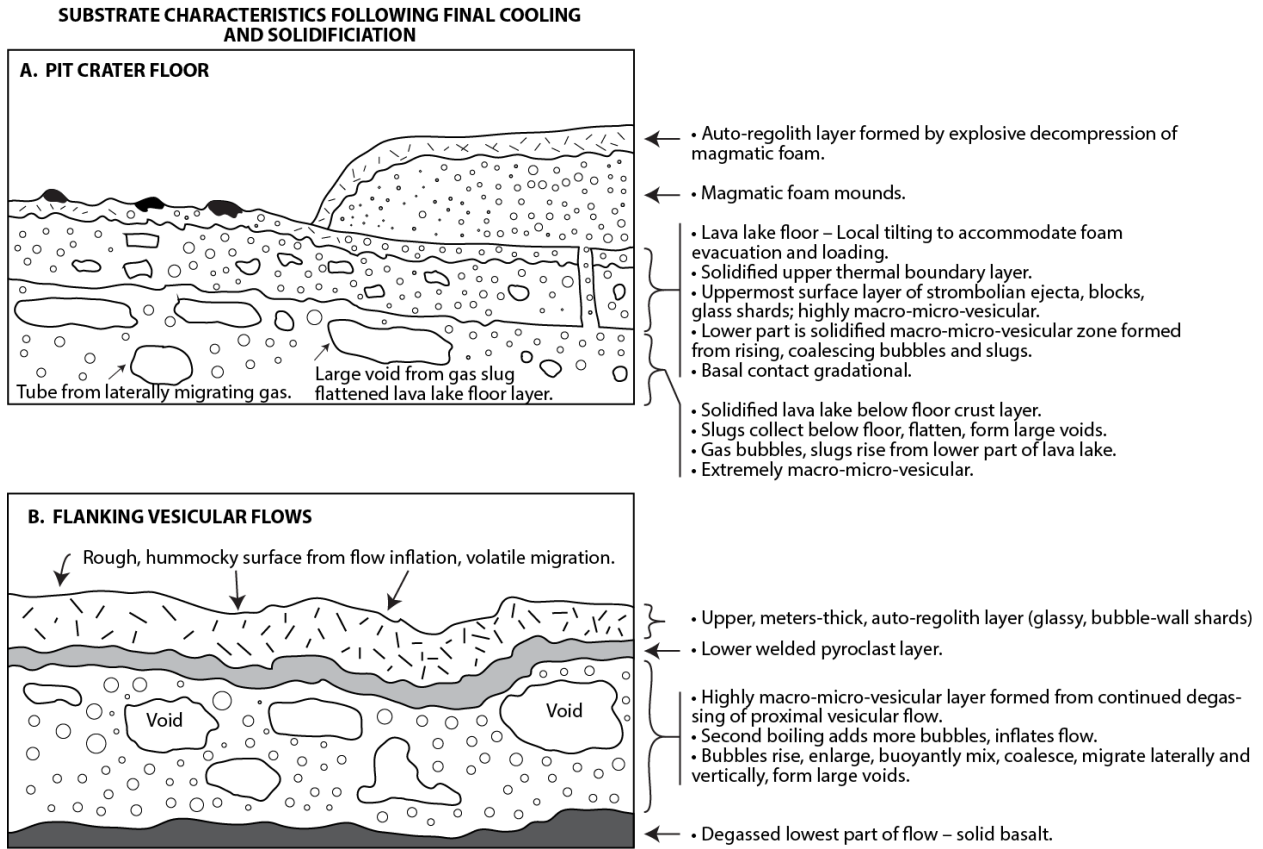
1144

Figure 12. The interpreted stages in the ascent, eruption, evolution and final cooling of the Cauchy 5 small shield volcano intrusive-extrusive event. (a) Dike approaches surface. (b) Dike tip penetrates to surface vacuum, explosively vents gas and foam, forms pit crater. (c) Low rise-rate, largely degassed magma below gas/foam in dike top rises to fill the newly formed pit crater, and overflows to form cooling limited basalt flows. (d) In the very abbreviated Phases 2 and 3 (relative to larger lava flows; Figure 11), the transition to Phase 4 activity occurs. (e) In Phase 4, the lava lake overflows, emplacing highly bubble-rich/vesicular lava flows on the shield flanks. (f) Lava recedes into the pit crater, forming a cooling and thickening lava lake surface layer. (g) As the lava lake floor layer thickens, strombolian activity is inhibited, and gas continues build-up below the floor as gas slugs, vesicles and foams. (h) As the lava lake cools, the floor layer cracks and magmatic foams in the upper lava lake extrude to form viscous-appearing mounds; the foam surface explosively decompresses, forming an auto-regolith layer. (i) Lava lake undergoes final cooling and subsidence.



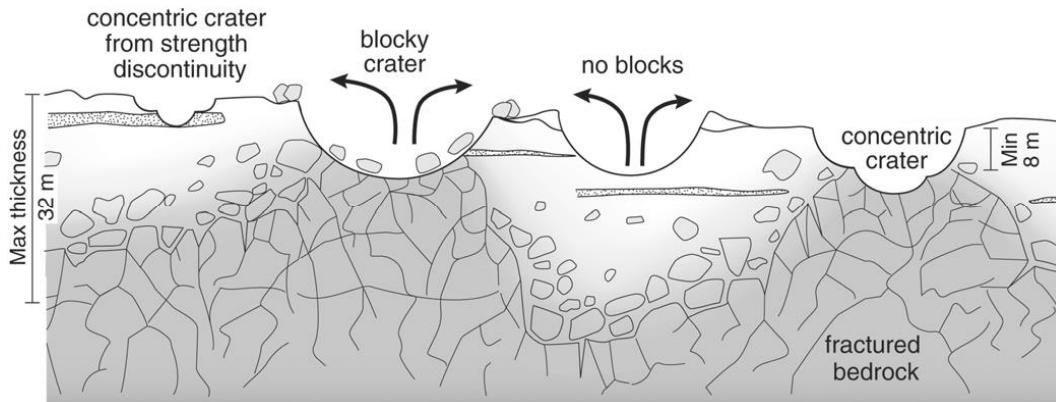
1145

1146 **Figure 13.** Map view of the stages in evolution of the Cauchy 5 small shield volcano. a) Upper
 1147 part of dike penetrates to the surface, catastrophically vents gas and foam into the vacuum,
 1148 causing collapse to form the elongate pit crater. b) Initial gas-depleted magma extrudes out of the
 1149 pit crater to form initial stages of small shield. c) Second phase of shield building involves rise of
 1150 gas-containing magma into the top of the dike and pit crater, significant degassing and bubble
 1151 growth, coalescence and rise, driving bubble-foam rich magma up over pit crater rim and onto
 1152 the shield flanks. d) As magma rise rate lowers and gas is further exsolved, volume decreases in
 1153 lava lake cause its lowering and retreat back into the pit crater. Drainage of lava below the north-
 1154 northwest part of the rim cause some parts of the chilled surface layer to flow back into the pit
 1155 crater, exposing the bubble rich middle flow, and causing additional gas loss and surface
 1156 evolution. e) In final stages of eruption, gas builds up below the lava lake floor thermal boundary
 1157 layer, foams are extruded through flexing and cracking of the floor, followed by final
 1158 solidification and floor subsidence.



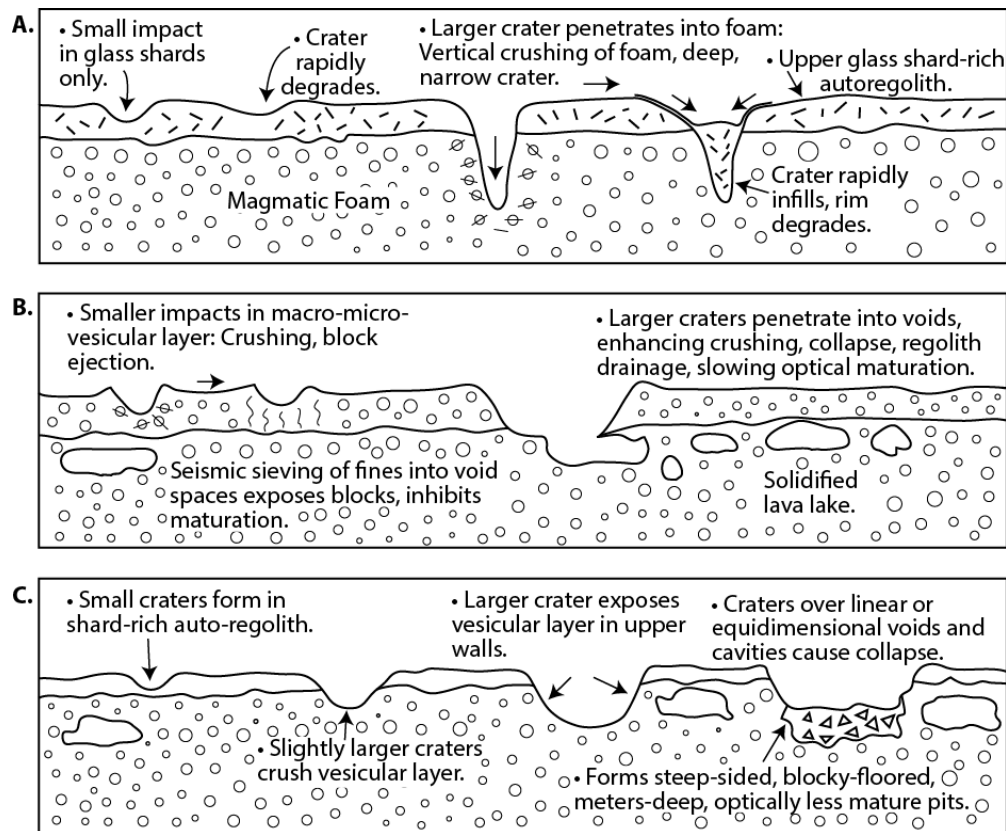
1159

1160 **Figure 14.** Detailed cross-section of the interpreted final configuration of the substrate in (a) the
 1161 Cauchy 5 pit crater interior and (b) the flanking bubble-rich/vesicular lava flows.



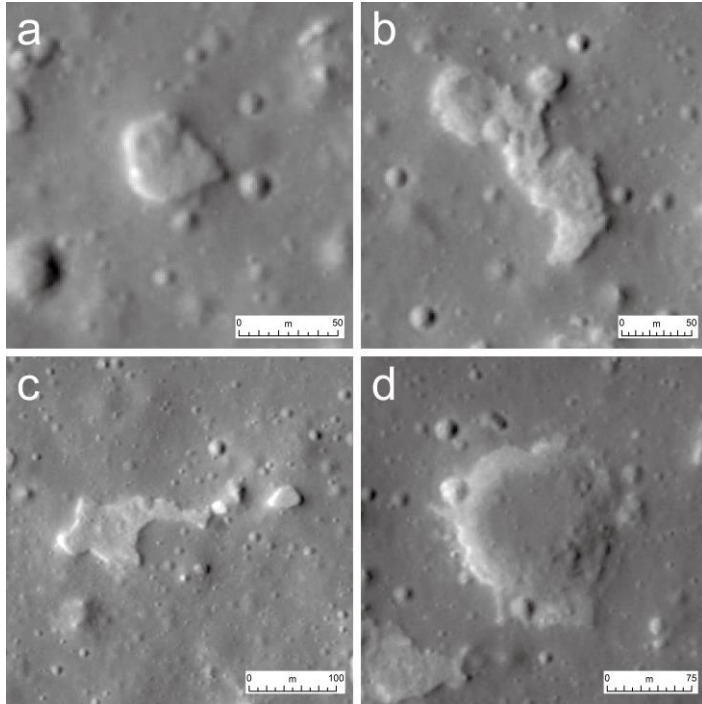
1162

1163 **Figure 15.** The typical model of lunar regolith development from uneven and fractured bedrock
 1164 surface, and the characteristics of superposed impact craters (from Wilcox et al., 2005 with kind
 1165 permission of John Wiley and Sons). Impact craters developed entirely in regolith will be non-
 1166 blocky, impacts into the bedrock will produce blocky craters, and impacts into a strength
 1167 discontinuity (typically regolith layer above bedrock) will result in concentric craters.



1168

1169 **Figure 16.** Nature of final substrates in the Cauchy 5 shield volcano and the implications for
 1170 superposed impact craters of various sizes and their evolution and degradation. (a) Mounds in the
 1171 Cauchy 5 pit crater interior and floor. (b) Rough floor areas of the pit crater interior. (c) Flanking
 1172 flows of the small shield. Note the unusual effects of superposed craters (e.g., Head & Ivanov,
 1173 2019; Ivanov & Head, 2019) and their degradation compared to those in solid basalt substrates
 1174 such as portrayed in Figure 15.



1175

1176 **Figure 17.** Examples of Type 2 IMPs on the Cauchy 5 small shield flanks and their interpreted
 1177 origins: a) impact-induced mechanical collapse of surface into underlying layer void space,
 1178 forming pits with a blocky immature deposit on the floor and exposing adjacent fresh layers in
 1179 the pit walls); b) shock-induced shattering of bubble and foam walls and collapse of overlying
 1180 layers producing depressions and pits that are highly irregular in shape; c) a variety of craters
 1181 with non-traditional morphologies, degradation states and morphometries due to lateral and
 1182 vertical variations in size and distribution of layer pore space and the effects on energy
 1183 partitioning; d) an even larger impact event that penetrate through the entire flanking flow into
 1184 the underlying solid basalt shield and regional mare substrate deposits, exposing the porous layer
 1185 in the upper part of their walls. All sub-panels are from LROC NAC frame M1108025067.